Article

Landscape of human antibody recognition of the SARS-CoV-2 receptor binding domain

Graphical abstract
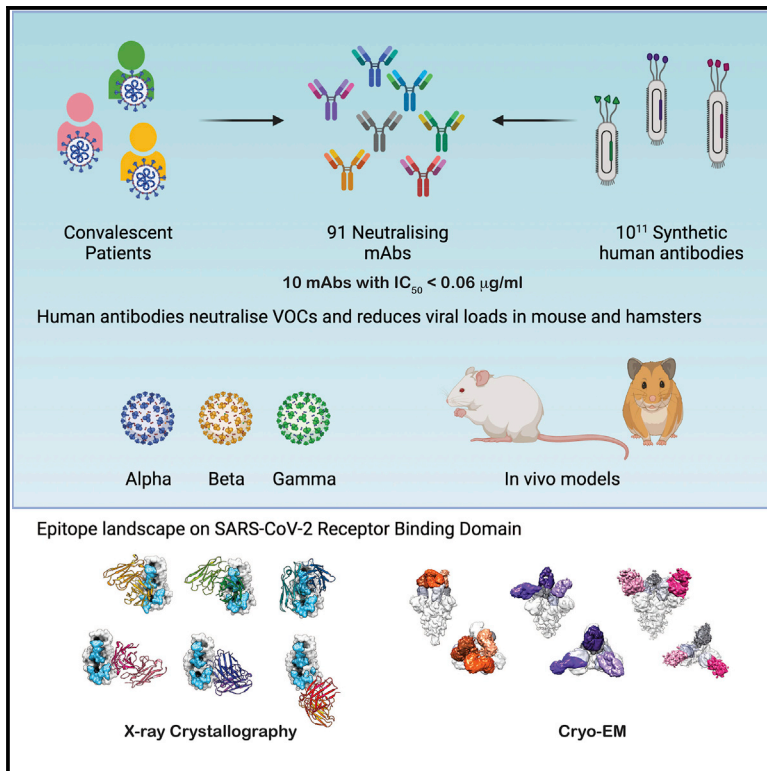
Authors
Adam K. Wheatley, Phillip Pymm, Robyn Esterbauer, ..., Kanta Subbarao, Stephen J. Kent, Wai-Hong Tham

Correspondence
skent@unimelb.edu.au (S.J.K.),
tham@wehi.edu.au (W.-H.T.)

In brief
Wheatley et al. identify potent human monoclonal antibodies that block SARS-CoV-2 virus entry and ameliorate SARS-CoV-2 infection in mice and hamsters. Structural analyses reveal the diverse epitope landscape of neutralizing antibodies that will be potentially useful in future anti-SARS-CoV-2 therapeutics.

Highlights

- Neutralizing monoclonal antibodies block SARS-CoV-2 virus entry

- Reduced SARS-CoV-2 infection in mice and hamsters

- Leading antibodies unaffected by VOCs, such as B1.1.7., B.1.351, and P.1

- Cryo-EM and crystallography reveal the epitope landscape of neutralizing antibodies

CelPress

Article

Landscape of human antibody recognition of the SARS-CoV-2 receptor binding domain

Adam K. Wheatley,[1,2,13] Phillip Pymm,[3,4,13] Robyn Esterbauer,[1] Melanie H. Dietrich,[3,4] Wen Shi Lee,[1] Damien Drew,[3,4] Hannah G. Kelly,[1] Li-Jin Chan,[3,4] Francesca L. Mordant,[1] Katrina A. Black,[3,4] Amy Adair,[3] Hyon-Xhi Tan,[1] Jennifer A. Juno,[1] Kathleen M. Wragg,[1] Thakshila Amarasena,[1] Ester Lopez,[1] Kevin J. Selva,[1] Ebene R. Haycroft,[1] James P. Cooney,[3,4] Hariprasad Venugopal,[5] Li Lynn Tan,[3] Matthew T. O Neill,[3] Cody C. Allison,[3,4] Deborah Cromer,[6] Miles P. Davenport,[6] Richard A. Bowen,[7] Amy W. Chung,[1] Marc Pellegrini,[3,4] Mark T. Liddament,[8] Alisa Glukhova,[3,4,9,10] Kanta Subbarao,[1,11] Stephen J. Kent,[1,2,12,14,*] and Wai-Hong Tham[3,4,14,15,*]

[1]Department of Microbiology and Immunology, University of Melbourne, the Peter Doherty Institute for Infection and Immunity, Melbourne, VIC 3000, Australia
[2]Australian Research Council Centre for Excellence in Convergent Bio-Nano Science and Technology, University of Melbourne, Melbourne, VIC 3010, Australia
[3]The Walter and Eliza Hall Institute of Medical Research, Parkville, VIC 3052, Australia
[4]Department of Medical Biology, The University of Melbourne, Melbourne, VIC 3010, Australia
[5]Department of Biochemistry and Molecular Biology, Monash University, Clayton, VIC 3800, Australia
[6]Kirby Institute, University of New South Wales, Kensington, NSW 2052, Australia
[7]Laboratory of Animal Reproduction and Biotechnology, Colorado State University, Fort Collins, CO 80523, USA
[8]CSL Limited, Parkville, VIC 3052, Australia
[9]Drug Discovery Biology, Monash Faculty of Pharmacy and Pharmaceutical Sciences, Monash University, Parkville VIC 3052, Australia
[10]Department of Biochemistry and Pharmacology, The University of Melbourne, Melbourne, VIC 3010, Australia
[11]WHO Collaborating Centre for Reference and Research on Influenza, The Peter Doherty Institute for Infection and Immunity, 792 Elizabeth Street, Melbourne, VIC 3000, Australia
[12]Melbourne Sexual Health Centre and Department of Infectious Diseases, Alfred Hospital and Central Clinical School, Monash University, Melbourne, VIC 3004, Australia
[13]These authors contributed equally
[14]Senior author
[15]Lead contact
*Correspondence: skent@unimelb.edu.au (S.J.K.), tham@wehi.edu.au (W.-H.T.)
https://doi.org/10.1016/j.celrep.2021.109822

SUMMARY

Potent neutralizing monoclonal antibodies are one of the few agents currently available to treat COVID-19. SARS-CoV-2 variants of concern (VOCs) that carry multiple mutations in the viral spike protein can exhibit neutralization resistance, potentially affecting the effectiveness of some antibody-based therapeutics. Here, the generation of a diverse panel of 91 human, neutralizing monoclonal antibodies provides an in-depth structural and phenotypic definition of receptor binding domain (RBD) antigenic sites on the viral spike. These RBD antibodies ameliorate SARS-CoV-2 infection in mice and hamster models in a dose-dependent manner and in proportion to *in vitro*, neutralizing potency. Assessing the effect of mutations in the spike protein on antibody recognition and neutralization highlights both potent single antibodies and stereotypic classes of antibodies that are unaffected by currently circulating VOCs, such as B.1.351 and P.1. These neutralizing monoclonal antibodies and others that bind analogous epitopes represent potentially useful future anti-SARS-CoV-2 therapeutics.

INTRODUCTION

The global spread of SARS-CoV-2 has sparked intense global research efforts to combat the significant health and economic effects of the pandemic. Monoclonal antibodies (mAbs) have demonstrated promise as treatments or prophylactic agents against other viral diseases, such as respiratory syncytial virus (RSV) (Rocca et al., 2021) and Ebola (Misasi and Sullivan, 2021). The extremely rapid isolation and characterization of mAbs for the treatment or prevention of COVID-19 has, to

date, yielded hundreds of fully human mAbs with potent antiviral neutralizing activity (Brouwer et al., 2020; Dejnirattisai et al., 2021; Liu et al., 2020; Robbiani et al., 2020; Rogers et al., 2020; Zost et al., 2020a). Neutralizing epitopes have been mapped across the viral spike, including the receptor binding domain (RBD) (Barnes et al., 2020b; Dejnirattisai et al., 2021), N-terminal domain (NTD) (Cerutti et al., 2021; McCallum et al., 2021), and S2 domain (Wang et al., 2021a), with the most potent neutralizing activity associated with mAbs that directly block RBD interaction with the human receptor angiotensin-converting enzyme 2

(ACE2) (Andreano et al., 2021; Graham et al., 2021; Zost et al., 2020b). Interestingly, stereotypic immunoglobulin gene arrangements shared among multiple individuals are a notable feature of the RBD-specific neutralizing antibody response to infection (Chen et al., 2021a; Nielsen et al., 2020; Robbiani et al., 2020) and immunization (Chen et al., 2021a) as well as for NTD-specific antibodies (Voss et al., 2021).

The rapid clinical development of SARS-CoV-2 antibody-based therapeutics (reviewed in Taylor et al. [2021]) has seen rapid progression of candidate mAbs through clinical trials, with two human mAb cocktails (casirivimab/imdevimab and bamlanivimab/etesevimab) and one monotherapy (bamlanivimab) conditionally approved for treatment of high-risk, ambulatory patients. However, some of these first-generation treatments suffer significant losses of neutralization potency in the face of ongoing viral evolution, with near-complete loss of activity against B.1.351 and P.1 SARS-CoV-2 variants of concern (VOCs) reported for many neutralizing human mAbs (Wang et al., 2021b; Wang et al., 2021c; Wang et al., 2021d; Zhou et al., 2021). There is an ongoing need to accurately identify and characterize antibody epitopes that consistently yield robust *in vitro* and *in vivo* neutralization outcomes across the critical viral spike protein. This should allow the selection of antibody cocktails for maximized protection against VOCs and inform rational improvements to the next generation of COVID-19 vaccines.

Here, we characterized 91 neutralizing human mAbs recovered either using phage library display or from convalescent COVID-19 subjects. Comprehensive structural analysis using X-ray crystallography and cryo-electron microscopy (cryo-EM) characterized the antigenic landscape of SARS-CoV-2 RBD, with both stereotypic and unique neutralizing epitopes identified and detailed antibody paratope-epitope interactions defined. Protective efficacy of single antibodies and cocktails was assessed both in mice using mouse-tropic SARS-CoV-2 variants and in Syrian hamster challenge models. Finally, the resilience of distinct epitope regions on the RBD to mutations observed in SARS-CoV-2 VOC was assessed, revealing structural insights into the drivers of loss or maintenance of virus neutralization.

RESULTS

Recovery of potent human neutralizing mAbs against SARS-CoV-2 spike

We previously described a cohort of individuals recovered from COVID-19 (Juno et al., 2020b) who developed serological binding and neutralizing antibodies against SARS-CoV-2 spike after recovery. From six donors (Figure S1A), we sorted single immunoglobulin G (IgG) memory B cells (CD19$^+$IgD$^-$IgG$^+$) that bound to SARS-CoV-2 spike and/or RBD probes and recovered recombined immunoglobulin gene sequences using multiplex RT-PCR (gating in Figure S1B). A total of 1,280 heavy-chain immunoglobulins, with 935 paired light chains, were recovered (Figure S1A), and 212 antibodies (denoted with the prefix PDI) were selected for expression in mammalian cell culture.

161 of 212 human mAbs expressed bound S or RBD (Table S1) and were further screened for neutralizing activity against the SARS-CoV-2 isolate hCoV-19/Australia/VIC01/2020 using a robust, limiting-dilution live-virus microneutralization format. 69
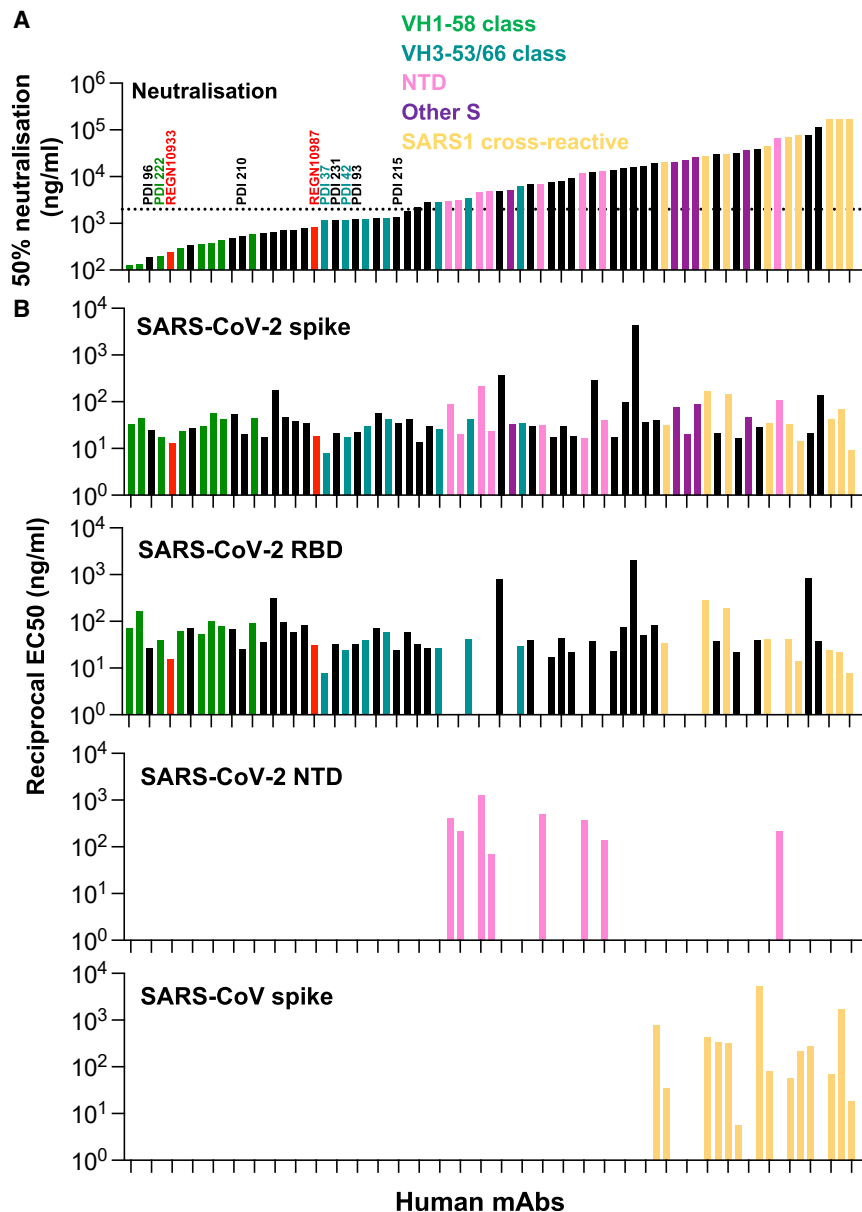
neutralizing mAbs were identified, with neutralization potency ranging from 127 ng/mL to 167 μg/mL (Figure 1A). Reactivity was assessed by ELISA for binding to SARS-CoV-2 spike (69/69), RBD (56/69), the NTD (8/69), or cross-reactive recognition of spike proteins from SARS-CoV-1 (13/69) (Figure 1B) or endemic human betacoronaviruses HKU1 (0/69) and OC43 (0/69) (data not shown). Sequence analysis of recovered immunoglobulins confirmed recurrent selection of previously described stereotypic antibody classes (Figure S1C), with VH3-53/3-66 (Barnes et al., 2020b; Robbiani et al., 2020; Yan et al., 2021) or VH1-58 (Chen et al., 2021a; Dejnirattisai et al., 2021) germlines featuring prominently among the most-potent RBD-specific mAbs. Overall, 26 mAbs showed high potency with an endpoint microneutralization titer of <2 μg/mL, comparable with well-characterized antibodies casirivimab (REGN10933) and imdevimab (REGN10987) (Hansen et al., 2020).

In parallel, we screened a semi-synthetic human Fab library with a diversity of 10^{11}, using SARS-CoV-2 spike or RBD. Of the 760 individual phage clones selected, we identified 121 unique clones, which we expressed recombinantly (Table S2). All phage-display human mAbs (denoted with the prefix WCSL) were also screened for neutralizing activity against the SARS-CoV-2 virus, with 22 neutralizing mAbs identified ranging in neutralization potency from 0.098 μg/mL to 3.1 μg/mL (Figure 2A). Reactivity was assessed by ELISA for binding to SARS-CoV-2 spike (109/121), SARS-CoV-2 RBD (58/121), or SARS-CoV RBD (16/121; Figures 2B–2D). Overall, 16 WCSL mAbs met our criteria demarking high potency with microneutralization endpoint titer <2 μg/mL.

Structural definition of the antigenic landscape of the RBD

A subset of 12 potently neutralizing RBD-specific mAbs representing diverse germline families (eight from convalescent donors and four from phage display) were down-selected for further functional and structural analyses. The binding characteristics of each antibody to the RBD was assessed using bio-layer interferometry (BLI), the capacity to block RBD interaction with ACE2 was assessed by ELISA, and potent neutralization activity was confirmed using both plaque-reduction neutralization titers (PRNTs) and an ELISA-based micro-neutralization readouts (Table S3). Epitope diversity was assessed by pairwise competition panning using BLI (Figure 3A). Based upon clustering patterns of mutual binding inhibition and subsequent structural analysis, we defined six putative epitope clusters distributed widely across the RBD surface (Figure 3B): cluster 1 (PDI 37, PDI 42, PDI 222, PDI 231, WCSL 120, WCSL 129, and REGN10933), cluster 2 (PDI 210), cluster 3 (WCSL 55 and WCSL 119), cluster 4 (PDI 215), cluster 5 (PDI 93), and cluster 6 (PDI 96 and REGN10987).

Structural analysis was carried out by X-ray crystallography using co-complex of Fabs bound to monomeric RBD (9 of 12 mAbs) (Tables S4 and S5) and by high-resolution cryo-EM using Fab bound to the trimeric spike (1 of 12 mAbs) (Table S6). Crystallographic datasets for antibodies were obtained in complex with RBD, and both PDI 93 and PDI 96 were obtained in co-complex with RBD and WCSL 129. Antibodies from all clusters displayed partial overlap of binding sites with that of ACE2, providing a mechanistic basis for potent neutralization activity

A

the public clonotype sequence signatures. The longer CDR-H3 loop is accommodated through an alteration of the conformation of the β-sheet and loop between K45 and G57, which is raised away from the RBD surface. This allows protrusion of the CDR H3 loop across the ACE2 binding surface of the RBD, without alteration of the approach angle of the antibody (Figures 3B and S2C). A previously reported VH3-53 antibody structure (COVA2-39) with an equivalent CDR-H3 length adopts a different angle of approach to the RBD, and the position of the heavy chain is rotated nearly 90° from VH3-53/66 binding mode 1.

Although not of the same gene usage (Table S2), WCSL 129 bound a similar epitope largely overlapping that of the VH3-53/66 class but with its center shifted slightly toward the RBD residue S477 (Figure S2B). Nevertheless, all of the RBD residue contacts of WCSL 129 fall within the epitope defined by the VH3-53/66 class antibodies with no contacts unique to WCSL 129 (Figure S2A). PDI 210 in cluster 2 also largely overlaps the epitope of the VH3-53/66 mAbs (Figure 3C), with a slightly larger heavy-chain footprint on the RBD (838.7 Å² compared with 765.6 Å² for PDI 37) contacting additional

(Figures 3B and S2A). PDI 231, PDI 37, PDI 42, and PDI 210 bound the RBD with similar angles of approach (Figure S2B) and had binding footprints that showed the most overlap with the ACE2 interaction site. PDI 231 and PDI 42 contact 14 RBD residues that form part of the ACE2 interaction site (Figure S2A).

Antibodies derived from germlines VH3-53 or VH3-66 with a short CDR-H3 of 9–12 residues comprise a stereotypic class commonly isolated from individuals after recovery from COVID-19 (Robbiani et al., 2020; Yan et al., 2021). Within cluster 1, mAbs PDI 37 and PDI 42 bound similarly to the previously characterized binding mode 1 (Barnes et al., 2020a) (Figure 3B) and fall within defined public clonotypes 1 and 2 (Tan et al., 2021). In contrast, PDI 231, although sharing VH3-53 gene usage, has a longer CDR-H3 at 16 residues (Table S1), which diverges from
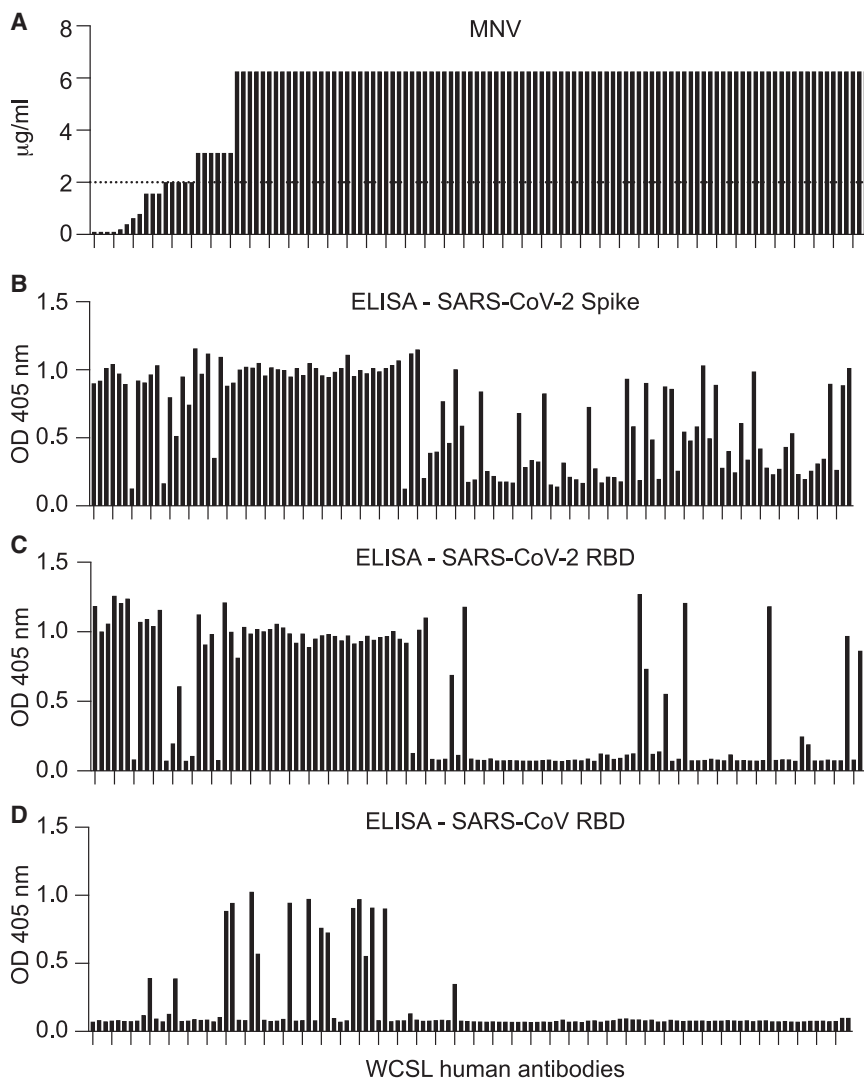
RBD residues Q498 and Y505, which form part of the RBD-ACE2 interface (Figure S2A).

PDI 222 is derived from a VH1-58 germline sequence that forms another stereotypic class of antibody isolated from convalescent COVID-19 patients (Chen et al., 2021a; Dejnirattisai et al., 2021; Dong et al., 2021; Kreer et al., 2020; Robbiani et al., 2020; Tortorici et al., 2020). The VH1-58 class has a well-defined epitope on the RBD, centered on the RBD residue N487 (Figures 3B and S2B) overlapping the ACE2 interaction site at fewer residues (7 versus 14) than the VH3-53/66 class antibodies PDI 37, PDI 42, and PDI 231 (Figure S2A).

WCSL 119 in cluster 3 bound an epitope centered on RBD residue E484 (Figure S2B), which partly overlaps with the ACE2 binding site, sharing eight RBD contacts (Figures 3B and S2A). The

Figure 2. Neutralization and specificity of SARS-CoV-2 RBD and spike-specific WCSL mAbs from phage display
(A) Neutralization of live SARS-CoV-2 virus (hCoV-19/Australia/VIC01/2020) was assessed for synthetic mAbs recovered from phage display (n = 120). Dashed line indicates the 2-μg/mL threshold used to define high potency.
(B–D) Binding to (B) recombinant SARS-CoV-2 trimeric spike, (C) monomeric SARS-CoV-2 RBD, or (D) monomeric SARS-CoV RBD. For (B)–(D), the bar graphs represent means of n = 2 biological replicates with n = 2 technical replicates.

(Figure S2C), with the closest approach of the light chain to the RBD being more than 6.5 Å (Figure 3B).

In agreement with the BLI analysis, PDI 93 (cluster 5) and PDI 96 (cluster 6) bound epitopes distal to cluster 1 and 2 mAbs (Figures 3C and S2B). These epitopes interact with fewer ACE2 contact residues than the antibodies in clusters 1–3, sharing only three (PDI 93) or two (PDI 96) contacts on the RBD (Figure S2A). PDI 96 largely overlaps the resolved epitope for REGN10987 (Hansen et al., 2020), although it has a light-chain CDR-L1 loop not found in REGN10987 that binds a cleft on the side of the RBD (Figure S2C). This forms additional hydrogen-bond interactions with the RBD N440 side chain and contacts the L441 and S373 side chains. The two contacts shared with the ACE2 epitope are at the top of the PDI 96 binding site at RBD residues G446 and T500 (Figures 3B and S2A).

The light chain of PDI 93 overlaps the light chain of the previously characterized C135 (Barnes et al., 2020a), although the orientation of the antibody results in an epitope sharing only 4 of 17 contact residues. A recently published antibody, COVOX 278 (Liu et al., 2021), contacts a similar epitope to PDI 93, sharing 17 of the 26 PDI 93 RBD contact residues; notably, a difference in positioning of the CDR-H3 loop in PDI 93 might allow for greater tolerance of the L452R mutation than is reported for COVOX 278. Neither chain of PDI 93 directly overlaps ACE2, although the heavy chain interacts with the ACE2 contact residues G446, Y449, and Q493 of the RBD (Figure S2A).

Antibody recognition in the context of the spike trimer
Fab binding in the context of the trimeric spike was assessed using cryo-EM. Datasets for PDI 93, PDI 96, PDI 210, PDI 215, PDI 222, WCSL 119, and WCSL 129 were collected at a resolution of 4.07–8.3 Å to allow determination of spike conformation and antibody occupancy (Table S6; Figures S3 and S4). Consistent with cryo-EM structures for other mAbs overlapping the ACE-2 binding motif
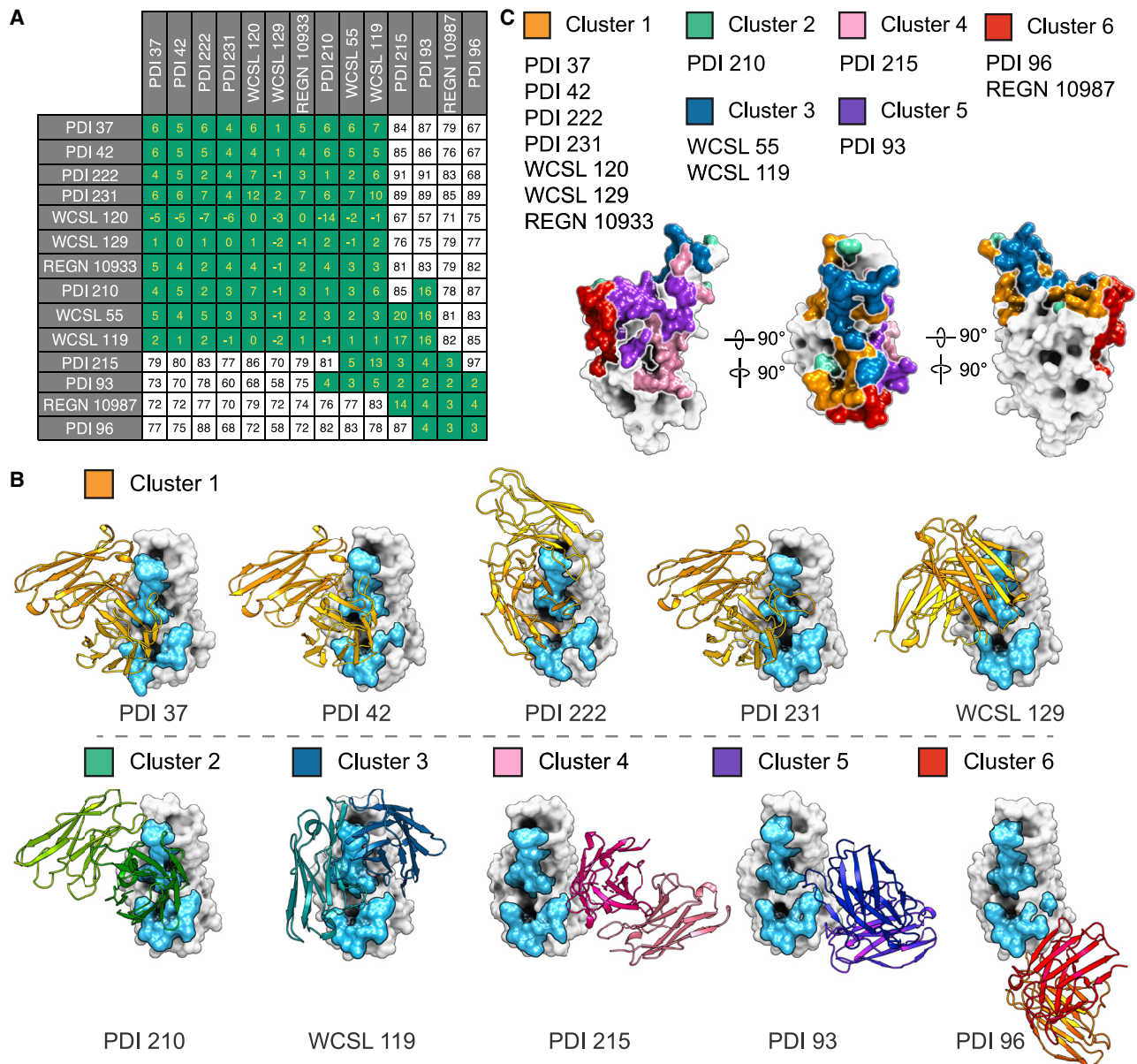
CDR-H1 and CDR-H3 and the CDR-L1 and CDR-L3 loops are responsible for most contacts with the RBD (Figure S2C). The VH1-2 heavy-chain gene usage is also reported to be enriched in response to SARS-CoV-2 RBD in convalescent subjects (Robbiani et al., 2020), with structures resolved to date falling into two binding modes (Yuan et al., 2021, Rapp et al., 2021). The WCSL 119 epitope overlaps that of previously reported VH1-2 binding modes, although the interactions and approach angle differ.

Interestingly, PDI 215 in cluster 4 bound a unique epitope on the distal face of the RBD (Figure 3C), a location consistent with an inability to inhibit ACE2 and RBD interaction in vitro, despite one shared interaction residue on the RBD Y449 (Table S3; Figure S2A). The inability to inhibit ACE2 binding places PDI 215 within the "class 3" RBD antibodies (Barnes et al., 2020a). The CDR-H3 loop of PDI 215 stretches down to contact RBD residue V341, more than 27 Å from the nearest ACE2 binding residue (Figure S2C). The interaction of PDI 215 with the RBD was also unusual in that it is driven entirely by the antibody heavy chain

A

	PDI 37	PDI 42	PDI 222	PDI 231	WCSL 120	WCSL 129	REGN 10933	PDI 210	WCSL 55	WCSL 119	PDI 215	PDI 93	REGN 10987	PDI 96
PDI 37	6	5	6	4	6	1	5	6	6	7	84	87	79	67
PDI 42	6	5	5	4	4	1	4	6	5	5	85	86	76	67
PDI 222	4	5	2	4	7	-1	3	1	2	6	91	91	83	68
PDI 231	6	6	7	4	12	2	7	6	7	10	89	89	85	89
WCSL 120	-5	-5	-7	-6	0	-3	0	-14	-2	-1	67	57	71	75
WCSL 129	1	0	1	0	1	-2	-1	2	-1	2	76	75	79	77
REGN 10933	5	4	2	4	4	-1	2	4	3	3	81	83	79	82
PDI 210	4	5	2	3	7	-1	3	1	3	6	85	16	78	87
WCSL 55	5	4	5	3	3	-1	2	3	2	3	20	16	81	83
WCSL 119	2	1	2	-1	0	-2	1	-1	1	1	17	16	82	85
PDI 215	79	80	83	77	86	70	79	81	5	13	3	4	3	97
PDI 93	73	70	78	60	68	58	75	4	3	5	2	2	2	2
REGN 10987	72	72	77	70	79	72	74	76	77	83	14	4	3	4
PDI 96	77	75	88	68	72	58	72	82	83	78	87	4	3	3

C

Cluster 1 — PDI 37, PDI 42, PDI 222, PDI 231, WCSL 120, WCSL 129, REGN 10933

Cluster 2 — PDI 210

Cluster 3 — WCSL 55, WCSL 119

Cluster 4 — PDI 215

Cluster 5 — PDI 93

Cluster 6 — PDI 96, REGN 10987

B

Cluster 1: PDI 37, PDI 42, PDI 222, PDI 231, WCSL 129

Cluster 2: PDI 210 — Cluster 3: WCSL 119 — Cluster 4: PDI 215 — Cluster 5: PDI 93 — Cluster 6: PDI 96

Figure 3. Defining RBD binding epitopes for lead candidate antibodies

(A) Epitope binning-competition BLI. Antibodies competing for RBD binding are shown in green; non-competitive antibody pairs are shown in white.

(B) Crystal structures of lead candidate antibody Fab in complex with the SARS-CoV-2 RBD (gray). The RBD is shown in surface representation, and the footprint of the ACE2 binding site is highlighted in blue. Antibody-variable domains are shown in cartoon representation and are colored by cluster.

(C) Surface representation of the SARS-CoV-2 RBD (gray) back face, top, and front face (left to right) showing the binding footprints for each of the six identified epitope clusters. Footprints for the ACE2 and antibody binding sites are defined by residue contacts within 4 Å of the SARS-CoV-2 RBD.

and previously grouped as "class 1" RBD antibodies (Barnes et al., 2020a; Brouwer et al., 2020; Dejnirattisai et al., 2021; Rogers et al., 2020), WCSL 129, PDI 210, and PDI 222 bound the RBD only in the up (open) conformation, with three antibodies bound to each spike trimer (Figures 4A–4C). In contrast, WCSL 119 bound the RBD in both up and down conformations with two of the RBDs up and a single RBD down (Figure 4D). The complex between PDI 215 and SARS-CoV-2 spike appeared unstable on our grids, with only 1% of particles containing an intact spike, which may

suggest a mode of neutralization for this antibody. PDI 215 is bound to two RBDs in the up conformation (Figure 4E), with the third RBD being disordered and with limited density visible for much of the RBD and antibody. PDI 93 and PDI 96, which bind to distal RBD epitopes, bound at all three RBDs simultaneously in a one-up and two-down conformation (Figures 4F and 4G), which is the most-prevalent conformation of this spike construct in the absence of an antibody (Hsieh et al., 2020). WCSL 119, PDI 93, and PDI 96 fall into the previously proposed "class 2"
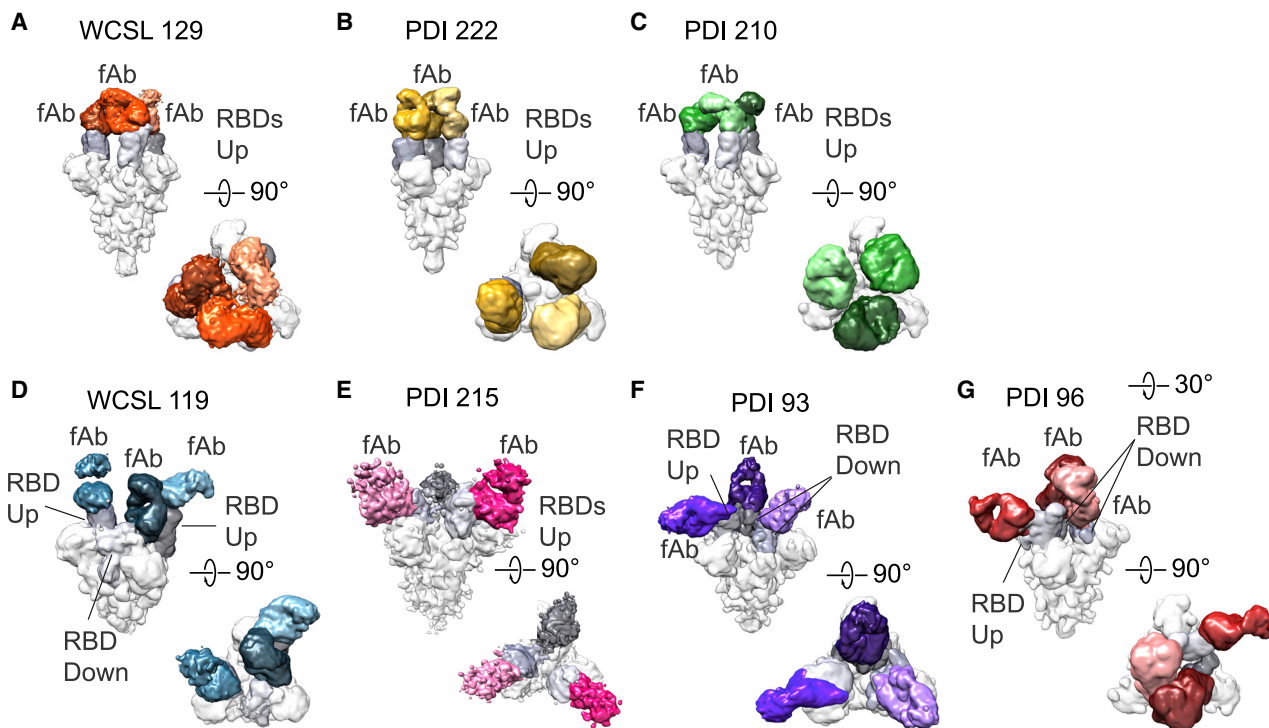
Figure 4. Structures of lead candidate Fabs with SARS-CoV-2 spike.
(A–G) Cryo-EM maps of Fab-spike complexes were lowpassed to 6 Å resolution with the spike (light gray), RBDs (darker grays), and Fab shown in their respective colors: (A) WCSL129 (orange), (B) PDI 222 (yellow), (C) PDI 210 (green), (D) WCSL 119 (blue), (E) PDI 215 (pink), (F) PDI 93 (purple), and (G) PDI 96 (red).

RBD antibodies (Barnes et al., 2020a), although they have very distinct epitopes on the RBD.

We recovered multiple highly potent antibodies from VH1-58 germlines, which have recently been identified as another stereotypic class in humans (Chen et al., 2021a; Dejnirattisai et al., 2021; Dong et al., 2021). High resolution cryo-EM of the PDI 222-spike complex shows an antibody-interaction site on the RBD consistent with the published structures of other VH1-58 class antibodies, COVOX-253 (Dejnirattisai et al., 2021) and S2E12 (Tortorici et al., 2020) (Figure S5). We similarly observed strong genetic conservation of key determinants, such as a di-cysteine motif within the CDR-H3, which is important for high-affinity binding of this clonotype to the SARS-CoV-2 RBD (Dong et al., 2021), and selection of near-identical VH3-20-derived κ chains.

Protective capacity of human mAbs in mice and hamsters
The capacity of mAbs to mediate antiviral activity *in vivo* was initially assessed using an isolate of SARS-CoV-2 (D614G N501Y) capable of supporting viral replication in wild-type (WT) mice (Pymm et al., 2021). Mice were given 5, 1, or 0.2 mg/kg doses of six different mAbs 1 day before an aerosolized challenge with SARS-CoV-2, with a primary endpoint of viral titers recoverable within lung homogenates. At 5 mg/kg, significant protection was afforded by all mAbs tested, with protection waning for most mAbs in line with dose (Figure 5A). Notably, a good correlation existed between *in vitro* microneutralization activity and lung viral titers in mice after treatment with the lowest dose of antibody, sug-

gesting neutralization potency is a key driver of *in vivo* protective potential (Figure 5B). Based on the robust protection observed as single agents, two cocktails, consisting of pairs of antibodies binding non-competing RBD epitopes, were selected: WCSL 119/PDI 96 (clusters 3 and 6) and PDI 222/PDI 96 (clusters 1 and 6). When used to prophylactically treat mice, both cocktails demonstrated potent protection at 1 mg/kg, comparable with the benchmark Regeneron cocktail, with some protective effects still observable at the low dose of 0.2 mg/kg (Figure 5C).

We next studied Syrian hamsters, a model with greater human-relevant pathogenesis, to further explore the potential of mAbs as treatments and prophylaxis of COVID-19. Antibodies PDI 222 and PDI 96 were delivered singly or in a cocktail via intraperitoneal injection 1 day before intranasal challenge with SARS-CoV-2, as previously described (Schäfer et al., 2021). Passive infusion at 5 mg/kg of each single antibody or a cocktail provided robust protection against SARS-CoV-2-induced weight loss (Figure 5D), with levels of virus at 3 days postinfection (dpi) virtually undetectable in the cranial (Figure 5E) or the caudal lung (Figure S6). Virus levels within nasal turbinates (3 dpi) or recovered from swabs (1–3 dpi) were dramatically reduced relative to animals dosed with isotype controls, suggesting accelerated viral clearance after challenge (Figure S6). Reduced protection was observed at 0.25 mg/kg dosing; however, an ~1.5-log reduction in viral levels in the lung and nasal passage and reduced weight loss were still evident. The contribution of Fc-mediated effector functions was assessed using variants of PDI 96 and PDI 222 modified with the inclusion of Leu234Ala/Leu235Ala (LALA) mutations proven to abrogate

and PDI 215); however, no additional protective benefit from inclusion of a third mAb was observed (Figure S6).

Gross pathology in the lung was assessed using hematoxylin and eosin staining on animals sacrificed at 3 and 7 dpi. We found infusion with 5 mg/kg PDI 96 or the PDI 96/222 cocktail provided robust protection against lung pathology associated with a SARS-CoV-2 challenge (Figure 5F), with PDI 222 providing moderate protection. Infusion with 0.25 mg/kg of either single or a cocktail of antibodies did not prevent lung pathology.

Epitope resilience of human mAbs in the context of SARS-CoV-2 VOC

The emergence of SARS-CoV-2 variants with reduced susceptibility to neutralization by antibodies is a significant confounder for currently authorized treatments. We first screened a panel of neutralizing mAbs (n = 40) for any loss of recognition to recombinant spike proteins from B.1.351, B.1.1.7, or P.1 VOCs. In line with other reports (Chen et al., 2021b; Wang et al., 2021c), a significant loss of binding to B.1.351 and P.1 VOCs was observed for approximately

Fc-receptor engagement across a wide range of species (Saunders, 2019). Both weight loss and viral levels in the lung were unchanged relative to the unmodified antibodies (Figure S6), suggesting protection is primarily driven by neutralization potency alone in this model. We similarly compared the protective capacity of a cocktail of three non-competing RBD mAbs (PDI 96, PDI 222,

(legend on next page)

one-third of anti-RBD mAbs, most strikingly those from the VH3-53/66 stereotypic class, including PDI 37, PDI 42, and WCSL 120 (Figure 6A). In contrast, binding to B.1.1.7 was largely unaffected. Recognition by NTD-specific neutralizing mAbs was compromised for B.1.351 (one of six still binding) and B.1.1.7 (two of six), whereas the recognition of P.1 was largely maintained (five of six).

Neutralizing activity was assessed using a virus-neutralization assay against WT and B.1.351 virus, with many antibodies displaying a significant loss of neutralization potency against B.1.351 (Figure 6B). Near-total loss of B.1.351 neutralization was observed for most of the VH3-53/66 stereotypic class and other selected RBD mAbs, including REGN10933. Structural analysis reveals such antibodies directly interact with one or more of positions 417, 484, and 501 of the RBD, which are substituted in the B.1.351 variant (Figure 6C). In the VH3-53/66, class PDI 37 forms hydrogen bonds and stacking interactions with the K417 side chain and hydrogen bonds with N501 (Figures 7A and 7B). Similarly, PDI 42 has stacking interactions against the K417 side chain and forms hydrogen bonds with both E484 and N501 side chains (Figures 7C and 7D), although these interactions would be lost with B.1.351.

Antibodies WCSL 119, WCSL 129, PDI 93, PDI 210, PDI 231, and PDI 215 directly contact at least one residue mutated in the VOC but suffer only a partial reduction (3–4-fold relative to WT) of neutralization potency (Figure 6C). Hydrogen bonds between WCSL 119 and RBD residue E484 are solely with the peptide backbone (Figure 7E), which may be less affected by substitution, whereas WCSL 129 forms hydrogen bonds with K417 (Figure 7F), although some of these might also be maintained with a K417N substitution. PDI 93 forms a hydrogen bond with residue E484, and PDI 210 forms Van der Waals contacts with RBD residues E484 and N501 (Figures 7G–7I). PDI 215 forms a salt bridge to RBD residue E484 (Figure 7J). PDI 231 makes direct contacts with the K417 and N501 side chains (Figures 7K and 7L); however, recognition of the RBD is likely maintained via longer CDR-H3 loop making additional contacts across the top surface of the RBD.

As expected, PDI 96- and REGN10987-binding epitopes, distal from the relevant E484K and K417N/T mutations (Figure 5C), bind VOCs and mediate potent neutralization of B.1.351. The resilience of REGN10987-like antibodies was further tested using a multiplex array of single amino-acid RBD changes observed in circulating viruses, with the glycine at position 446 of the RBD flagged as a critical residue for epitope recognition (Table S7).

Finally, all antibodies from the VH1-58 stereotypic class (PDI 222, PDI 209, and PDI 204) maintain broad recognition of VOCs and potent neutralization of B.1.351. Structural analysis shows that, although antibody PDI 222, as well as published

VH1-58 antibodies COVOX-253 and S2E12, all bind a shared epitope near the E484 and K417 residues (Figure S5), the only interaction is a hydrogen bond to the backbone carbonyl oxygen (Figure 7M). None of the VH1-58 class antibodies directly contact the side chains of those residues or the residue N501, which is substituted in B.1.351, B.1.1.7, and P.1.

DISCUSSION

Significant global research effort has yielded many promising antibodies and antibody-based biologics for prophylaxis or treatment of COVID-19. The utility of combining two or more antibodies into cocktails to limit the selection of viral escape mutants has been established *in vitro* (Baum et al., 2020b; Weisblum et al., 2020). Now, in the context of emerging VOCs, antibody cocktails also provide a logical strategy for redundant protection in the face of ongoing viral evolution. However, the parameters for optimal cocktail selection remain unclear. Here, using library-panning approaches and targeted isolation from convalescent subjects, we characterized a diverse panel of 92 neutralizing human mAbs and included a comprehensive structural analysis of a subset. Highly potent mAbs bound one of up to six putative epitope clusters localized across all faces of the RBD, which, except for PDI 215, efficiently blocked engagement of the cellular receptor ACE2. Single antibodies from a range of different epitope clusters were tested for antiviral effect *in vivo* using a murine challenge model, with all mAbs tested displaying some degree of protection at high dose. The extent of viral suppression correlated with *in vitro* measurements of neutralizing activity but not binding affinity, suggesting functional potency is a key defining metric for protective efficacy. Combinations of two non-competing RBD-specific antibodies have reached late-stage clinical development or approval (Baum et al., 2020a; Jones et al., 2021; Zost et al., 2020a), and we observed strong protective effects after prophylactic administration of analogous cocktails in mice and hamsters. The most-potent combination was structurally comparable with the Regeneron cocktail and comprised mAb PDI 96 binding a REGN10987-like epitope, and PDI 222, a VH1-58 class antibody binding the upper RBD. The inclusion of a third non-competing antibody (PDI 215), albeit with comparatively lower *in vitro* neutralization potency, did not enhance protection *in vivo*, suggesting maintenance of maximal potency is paramount. However, there may still be some combinatorial advantages for a three or more mAb cocktail binding diverse epitopes, by allowing for two or more active agents to be maintained in the face of VOCs and, thereby, limiting the *de novo* emergence of escape variants in treatment settings. A dependence for mAb interactions with Fc-receptor (FcR) bearing immune effector cells has been established for maximal protection *in vivo* for some RBD-specific mAbs in

---

Figure 6. Epitope resilience of mAbs in the context of SARS-CoV-2 variants

(A) Relative ELISA binding activity was determined for a panel of human mAbs (n = 40) using recombinant trimeric spike proteins from wild-type and B.1.1.7, B.1.351, and P.1 variants of concern.

(B) Comparison of neutralization potencies (half-maximal inhibitory concentration [IC$_{50}$] in ng/mL) for selected mAbs against wild-type and B.1.351 virus isolates. Bars represent geometric means ± SD titers of two assays.

(C) Human antibody footprints for lead candidates showing heavy- and light-chain contacts on the RBD surface (light chain in lighter color for each antibody). Contacts are shown for atoms within 4 Å of the RBD surface. Residues mutated in the variants of concern (VOCs) are labeled and colored in blue-black; where the antibody footprint overlaps a VOC, the contacted atoms are shown in violet.
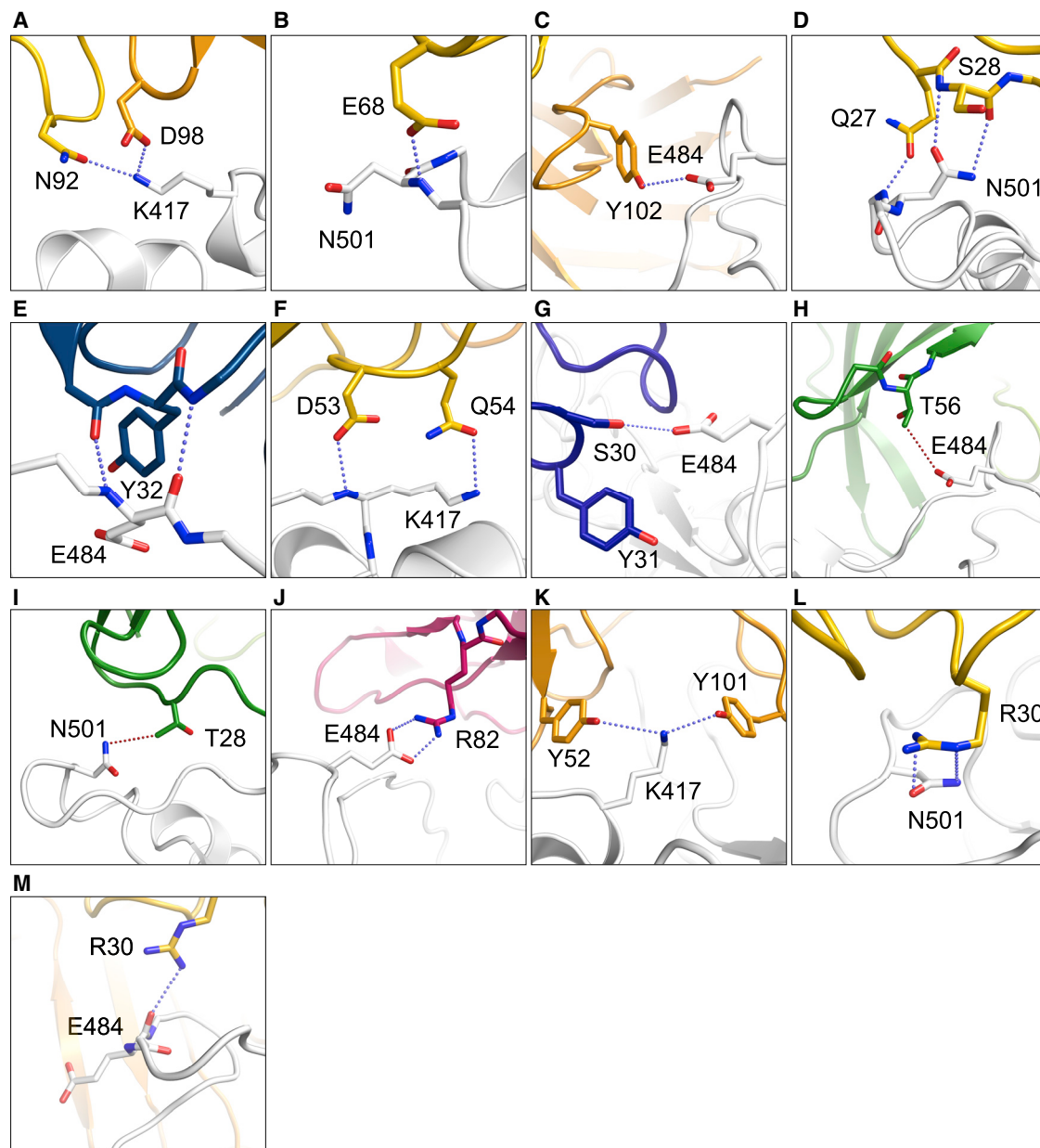
Figure 7. Interactions of structurally characterized lead candidates with RBD residues mutated in variants B.1.1.7, B.1.351, and P1

The RBD is shown in gray with antibodies shown in color: PDI 37, PDI 42, WCSL 129, and PDI 231 are in yellow (light chain) and orange (heavy chain); WCSL 119 in teal (heavy chain); PDI 93 in blue (heavy chain); PDI 210 in green (heavy chain) and light green (light chain); and PDI 215 shown in warm pink (heavy chain). Hydrogen bonds are shown in gray-blue; Van der Waals (VDW) interactions are shown in red.

(A) PDI 37 hydrogen bond with RBD residue K417.

(B) PDI 37 hydrogen bonds with RBD residue N501.

(C) PDI 42 hydrogen bond with RBD residue E484.

(D) PDI 42 hydrogen bonds with RBD residue N501.

(E) WCSL 119 forms two hydrogen bonds with the backbone of RBD residue E484.

(F) WCSL 129 hydrogen bonds with RBD residue K417.

(G) PDI 93 hydrogen bond with RBD residue E484.

(H) PDI 210 VDW interaction with RBD residue E484.

(I) PDI 210 VDW interaction with RBD residue N501.

(J) PDI 215 salt bridge with RBD residue R82.

(K) PDI 231 hydrogen bonds with RBD residue K417.

(L) PDI 231 hydrogen bonds with RBD residue N501.

(M) PDI 222 forms a hydrogen bond with the backbone of RBD residue E484.

mice (Schäfer et al., 2021). However, we find no reductions in protective capacity for the PDI 222/PDI 96 cocktail in hamsters, although it remains to be confirmed whether prototypic LALA mutations in the human IgG1 Fc abrogates FcR engagement in this model. In addition, antibody-FcR engagement has been reported to be of greater importance in treatment settings than when used as a prophylaxis (Winkler et al., 2021).

Epitope resilience in the face of emerging VOCs is a key concern for antibody-based antiviral agents, with both casirivimab (REGN10933; Regeneron) and bamlanivimab (LyCo555; Eli Lilly) reported to lose activity against B.1.351, in particular (Wang et al., 2021c). We similarly observe loss of recognition and/or neutralizing activity against B.1.351 and P.1 VOCs for nearly one-half of the mAbs tested. The effect was greatest for the widely prevalent VH3-53/66 class of RBD-specific antibodies and for NTD-specific mAbs in which the deletions and mutations reported in VOCs appear to alter the structural conformation of this domain (Kemp et al., 2020; McCallum et al., 2021). The combined effect of antigenic changes in RBD and NTD likely underpin the dramatic loss of neutralizing activity reported for polyclonal antibody responses in convalescent subjects and vaccine recipients (Greaney et al., 2021a, 2021b, 2021c; Voss et al., 2021; Wang et al., 2021c; Zhou et al., 2021).

So where best to target antibodies to maintain broad protection? Epitopes distal to the critical changes in the RBD at E484 and K417 carried by both B1.351 and P1 VOC, such as those bound by REGN10987-like antibodies (C135 [Barnes et al., 2020b] and PDI 96), show consistent recognition and neutralization of VOCs. However, mutagenesis suggests that substitutions at G446, although not widely prevalent in circulating virus strains, could potentially drive escape from such mAbs. Encouragingly, the stereotypic VH1-58 class of mAbs appears resistant to E484 and K417 changes in the RBD. Structurally, this class of antibodies, although binding proximally to both the K417 and E484 RBD residues, do not form contacts with either side chain and, therefore, maintain inhibition of ACE2 binding to current SARS-CoV-2 VOCs. Similarly, structure-based prediction suggests such mAbs would also be resistant in the face of L452 mutations as carried by fast-emerging B.1.617 variants.

The exceptional and conserved potency for the VH1-58 class of mAbs, observed in reported mAbs (Dejnirattisai et al., 2021; Robbiani et al., 2020; Zost et al., 2020a) and found in multiple donors in this study, suggests this common epitope abridging the ACE2 interaction site is a durable target for broad immunity in the face of viral variants. Elicitation of analogous responses by vaccination, in conjunction with REGN10987-like specificities, is a major consideration for engineering spike immunogens for robust protection in the face of ongoing viral evolution. The in-depth understanding of recognition and escape at key neutralizing epitopes is critical both for the next-generation of antibody-based therapeutic and prophylactic agents and for tailoring future COVID-19 vaccines to maximize immune focus onto conserved protective sites.

STAR★METHODS

Detailed methods are provided in the online version of this paper and include the following:

- ● KEY RESOURCES TABLE
- ● RESOURCE AVAILABILITY
  - ○ Lead contact
  - ○ Materials availability
  - ○ Data and code availability
- ● EXPERIMENTAL MODEL AND SUBJECT DETAILS
  - ○ Human subjects
  - ○ Mice
  - ○ Hamsters
  - ○ Cell lines
- ● METHOD DETAILS
  - ○ Sample collection
  - ○ Generation of recombinant proteins
  - ○ Limiting dilution microneutralisation assay
  - ○ Recovery of human monoclonal antibodies from SARS-CoV-2-specific B cells
  - ○ Phage library isolation of SARS-CoV-2 spike and RBD antibodies
  - ○ Screening ELISA for phage library mAbs
  - ○ Assessment of mAb binding specificity by ELISA
  - ○ ACE2-RBD inhibition ELISA
  - ○ Microneutralisation assay with ELISA-based read out
  - ○ Affinity measurements using bio-layer interferometry
  - ○ Two-way competition bio-layer interferometry for epitope assignment
  - ○ Plaque reduction neutralization assay
  - ○ Variant RBD Multiplex array
  - ○ Prophylaxis studies in mice using SARS-CoV-2 D614G N501Y virus
  - ○ Measurement of viral burden in SARS-CoV-2 infected mice
  - ○ Prophylaxis studies in hamsters
  - ○ Crystallography
  - ○ Cryo-EM sample preparation and data acquisition
  - ○ Cryo-EM data processing
  - ○ High resolution data processing for PDI 222
  - ○ Model building
  - ○ Statistical analyses

AUTHOR CONTRIBUTIONS

P.P. expressed and purified recombinant proteins and prepared samples for X-ray crystallography, crystallized RBD-WCSL Fab complexes, and collected diffraction data. M.H.D. with P.P., L.L.T., and L.-J.C. performed all the structural refinement for the crystal structures of RBD-Fab. D.D. performed the bio-panning using phage display and clonal analyses for WCSL antibodies and ELISA for specificity. A.A. performed the PRNT assays. L.-J.C. performed all bio-layer interferometry measurements for affinities and epitope competition, and established the FRET assay. J.P.C. performed the mouse experiments with the assistance of C.C.A. and the micro-neutralization assays for the WCSL antibodies. M.T.O., L.L.T., M.H.D., and D.D. assisted with expression and purification of recombinant proteins, WCSL antibodies, and the RBD variants. For cryo-EM, A.G., with the assistance of P.P., K.A.B., and H.V., prepared the samples, collected the data, and performed the data processing and model building. A.K.W. led human antibody recovery from convalescent individuals and drafted the manuscript. H.-X.T. performed single cell sorting of SARS-CoV-2-specific B cells. J.A.J., K.M.W., and S.J.K. recruited human subjects and processed blood samples. R.E., H.G.K., and T.A. cloned, expressed, and purified proteins and antibodies. W.S.L., F.L.M., and K.S. organized and performed live virus neutralization assays. E.L., K.J.S., E.R.H., and A.W.C. organized and performed multiplex RBD binding analysis. D.C. and M.P.D. provided statistical and high-level analytical support. R.A.B. led Syrian hamster studies. M.T.L. supervised the phage display, supplied RBD protein, provided high-level data analysis support, and led scaled-up antibody production to support animal studies. W.-H.T. and S.J.K. conceived the project, drafted the manuscript, and supervised the overall project. All authors assisted in manuscript preparation.

DECLARATION OF INTERESTS

REFERENCES

Amanat, F., Stadlbauer, D., Strohmeier, S., Nguyen, T.H.O., Chromikova, V., McMahon, M., Jiang, K., Arunkumar, G.A., Jurczyszak, D., Polanco, J., et al. (2020). A serological assay to detect SARS-CoV-2 seroconversion in humans. Nat Med 26, 1033–1036.

Andreano, E., Nicastri, E., Paciello, I., Pileri, P., Manganaro, N., Piccini, G., Manenti, A., Pantano, E., Kabanova, A., Troisi, M., et al. (2021). Extremely potent human monoclonal antibodies from COVID-19 convalescent patients. Cell 184, 1821–1835.e1816.

Argiriadi, M.A., Benatuil, L., Dubrovska, I., Egan, D.A., Gao, L., Greischar, A., Hardman, J., Harlan, J., Iyer, R.B., Judge, R.A., et al. (2019). CD40/anti-CD40 antibody complexes which illustrate agonist and antagonist structural switches. BMC Mol. Cell Biol. 20, 29.

Barnes, C.O., Jette, C.A., Abernathy, M.E., Dam, K.A., Esswein, S.R., Gristick, H.B., Malyutin, A.G., Sharaf, N.G., Huey-Tubman, K.E., Lee, Y.E., et al. (2020a). SARS-CoV-2 neutralizing antibody structures inform therapeutic strategies. Nature 588, 682–687.

Barnes, C.O., West, A.P., Jr., Huey-Tubman, K.E., Hoffmann, M.A.G., Sharaf, N.G., Hoffman, P.R., Koranda, N., Gristick, H.B., Gaebler, C., Muecksch, F., et al. (2020b). Structures of human antibodies bound to SARS-CoV-2 spike reveal common epitopes and recurrent features of antibodies. Cell 182, 828–842.e16.

Baum, A., Ajithdoss, D., Copin, R., Zhou, A., Lanza, K., Negron, N., Ni, M., Wei, Y., Mohammadi, K., Musser, B., et al. (2020a). REGN-COV2 antibodies prevent and treat SARS-CoV-2 infection in rhesus macaques and hamsters. Science 370, 1110–1115.

Baum, A., Fulton, B.O., Wloga, E., Copin, R., Pascal, K.E., Russo, V., Giordano, S., Lanza, K., Negron, N., Ni, M., et al. (2020b). Antibody cocktail to SARS-CoV-2 spike protein prevents rapid mutational escape seen with individual antibodies. Science 369, 1014–1018.

Brouwer, P.J.M., Caniels, T.G., van der Straten, K., Snitselaar, J.L., Aldon, Y., Bangaru, S., Torres, J.L., Okba, N.M.A., Claireaux, M., Kerster, G., et al. (2020). Potent neutralizing antibodies from COVID-19 patients define multiple targets of vulnerability. Science 369, 643–650.

Cerutti, G., Guo, Y., Zhou, T., Gorman, J., Lee, M., Rapp, M., Reddem, E.R., Yu, J., Bahna, F., Bimela, J., et al. (2021). Potent SARS-CoV-2 neutralizing antibodies directed against spike N-terminal domain target a single supersite. Cell Host Microbe 29, 819–833.e7.

Chen, E.C., Gilchuk, P., Zost, S.J., Suryadevara, N., Winkler, E.S., Cabel, C.R., Binshtein, E., Sutton, R.E., Rodriguez, J., Day, S., et al. (2021a). Convergent antibody responses to the SARS-CoV-2 spike protein in convalescent and vaccinated individuals. bioRxiv.

Chen, R.E., Zhang, X., Case, J.B., Winkler, E.S., Liu, Y., VanBlargan, L.A., Liu, J., Errico, J.M., Xie, X., Suryadevara, N., et al. (2021b). Resistance of SARS-CoV-2 variants to neutralization by monoclonal and serum-derived polyclonal antibodies. Nat. Med. 27, 717–726.

Chin, S.M., Kimberlin, C.R., Roe-Zurz, Z., Zhang, P., Xu, A., Liao-Chan, S., Sen, D., Nager, A.R., Oakdale, N.S., Brown, C., et al. (2018). Structure of the 4-1BB/4-1BBL complex and distinct binding and functional properties of uto-milumab and urelumab. Nat. Commun. 9, 4679.

Dejnirattisai, W., Zhou, D., Ginn, H.M., Duyvesteyn, H.M.E., Supasa, P., Case, J.B., Zhao, Y., Walter, T.S., Mentzer, A.J., Liu, C., et al. (2021). The antigenic anatomy of SARS-CoV-2 receptor binding domain. Cell 184, 2183–2200.e22.

Dong, J., Zost, S.J., Greaney, A.J., Starr, T.N., Dingens, A.S., Chen, E.C., Chen, R.E., Case, J.B., Sutton, R.E., Gilchuk, P., et al. (2021). Genetic and structural basis for recognition of SARS-CoV-2 spike protein by a two-antibody cocktail. bioRxiv.

Du, S., Cao, Y., Zhu, Q., Yu, P., Qi, F., Wang, G., Du, X., Bao, L., Deng, W., Zhu, H., et al. (2020). Structurally resolved SARS-CoV-2 antibody shows high efficacy in severely infected hamsters and provides a potent cocktail pairing strategy. Cell 183, 1013–1023.e13.

Emsley, P., Lohkamp, B., Scott, W.G., and Cowtan, K. (2010). Features and development of Coot. Acta Crystallogr. D Biol. Crystallogr. 66, 486–501.

Esswein, S.R., Gristick, H.B., Jurado, A., Peace, A., Keeffe, J.R., Lee, Y.E., Voll, A.V., Saeed, M., Nussenzweig, M.C., Rice, C.M., et al. (2020). Structural

basis for Zika envelope domain III recognition by a germline version of a recurrent neutralizing antibody. Proc. Natl. Acad. Sci. USA 117, 9865–9875.

Graham, C., Seow, J., Huettner, I., Khan, H., Kouphou, N., Acors, S., Winstone, H., Pickering, S., Galao, R.P., Dupont, L., et al. (2021). Neutralization potency of monoclonal antibodies recognizing dominant and subdominant epitopes on SARS-CoV-2 Spike is impacted by the B.1.1.7 variant. Immunity 54, 1276–1289.e6.

Greaney, A.J., Loes, A.N., Gentles, L.E., Crawford, K.H.D., Starr, T.N., Malone, K.D., Chu, H.Y., and Bloom, J.D. (2021a). Antibodies elicited by mRNA-1273 vaccination bind more broadly to the receptor binding domain than do those from SARS-CoV-2 infection. Sci. Transl. Med. 13, eabi9915.

Greaney, A.J., Starr, T.N., Barnes, C.O., Weisblum, Y., Schmidt, F., Caskey, M., Gaebler, C., Cho, A., Agudelo, M., Finkin, S., et al. (2021b). Mutational escape from the polyclonal antibody response to SARS-CoV-2 infection is largely shaped by a single class of antibodies. bioRxiv.

Greaney, A.J., Starr, T.N., Gilchuk, P., Zost, S.J., Binshtein, E., Loes, A.N., Hilton, S.K., Huddleston, J., Eguia, R., Crawford, K.H.D., et al. (2021c). Complete mapping of mutations to the SARS-CoV-2 spike receptor-binding domain that escape antibody recognition. Cell Host Microbe 29, 44–57.e9.

Hansen, J., Baum, A., Pascal, K.E., Russo, V., Giordano, S., Wloga, E., Fulton, B.O., Yan, Y., Koon, K., Patel, K., et al. (2020). Studies in humanized mice and convalescent humans yield a SARS-CoV-2 antibody cocktail. Science 369, 1010–1014.

Hsieh, C.L., Goldsmith, J.A., Schaub, J.M., DiVenere, A.M., Kuo, H.C., Javanmardi, K., Le, K.C., Wrapp, D., Lee, A.G., Liu, Y., et al. (2020). Structure-based design of prefusion-stabilized SARS-CoV-2 spikes. Science 369, 1501–1505.

Jardine, J.G., Kulp, D.W., Havenar-Daughton, C., Sarkar, A., Briney, B., Sok, D., Sesterhenn, F., Ereño-Orbea, J., Kalyuzhniy, O., Deresa, I., et al. (2016). HIV-1 broadly neutralizing antibody precursor B cells revealed by germline-targeting immunogen. Science 351, 1458–1463.

Jones, B.E., Brown-Augsburger, P.L., Corbett, K.S., Westendorf, K., Davies, J., Cujec, T.P., Wiethoff, C.M., Blackbourne, J.L., Heinz, B.A., Foster, D., et al. (2021). The neutralizing antibody, LY-CoV555, protects against SARS-CoV-2 infection in nonhuman primates. Sci. Transl. Med. 13, eabf1906.

Juno, J.A., Tan, H.-X., Lee, W.S., Reynaldi, A., Kelly, H.G., Wragg, K., Esterbauer, R., Kent, H.E., Batten, C.J., Mordant, F.L., et al. (2020a). Immunogenic profile of SARS-CoV-2 spike in individuals recovered from COVID-19. medRxiv. https://doi.org/10.1101/2020.05.17.20104869.

Juno, J.A., Tan, H.X., Lee, W.S., Reynaldi, A., Kelly, H.G., Wragg, K., Esterbauer, R., Kent, H.E., Batten, C.J., Mordant, F.L., et al. (2020b). Humoral and circulating follicular helper T cell responses in recovered patients with COVID-19. Nat. Med. 26, 1428–1434.

Kabsch, W. (2010). XDS. Acta Crystallogr. D Biol. Crystallogr. 66, 125–132.

Kaufmann, B., Vogt, M.R., Goudsmit, J., Holdaway, H.A., Aksyuk, A.A., Chipman, P.R., Kuhn, R.J., Diamond, M.S., and Rossmann, M.G. (2010). Neutralization of West Nile virus by cross-linking of its surface proteins with Fab fragments of the human monoclonal antibody CR4354. Proc. Natl. Acad. Sci. USA 107, 18950–18955.

Kemp, S.A., Collier, D.A., Datir, R., Ferreira, I., Gayed, S., Jahun, A., Hosmillo, M., Rees-Spear, C., Mlcochova, P., Lumb, I.U., et al. (2020). Neutralising antibodies in Spike mediated SARS-CoV-2 adaptation. medRxiv. https://doi.org/10.1101/2020.12.05.20241927.

Krissinel, E., and Henrick, K. (2007). Inference of macromolecular assemblies from crystalline state. J. Mol. Biol. 372, 774–797.

Kreer, C., Zehner, M., Weber, T., Ercanoglu, M.S., Gieselmann, L., Rohde, C., Halwe, D., Korenkov, M., Schommers, P., Vanshylla, K., et al. (2020). Longitudinal isolation of potent near-germline SARS-CoV-2-neutralizing antibodies from COVID-19 patients. Cell 182, 843–854.e12.

Liebschner, D., Afonine, P.V., Baker, M.L., Bunkóczi, G., Chen, V.B., Croll, T.I., Hintze, B., Hung, L.W., Jain, S., McCoy, A.J., et al. (2019). Macromolecular structure determination using X-rays, neutrons and electrons: recent developments in Phenix. Acta Crystallogr. D Struct. Biol. 75, 861–877.

Liu, S., Desharnais, J., Sahasrabudhe, P.V., Jin, P., Li, W., Oates, B.D., Shanker, S., Banker, M.E., Chrunyk, B.A., Song, X., et al. (2016). Inhibiting complex IL-17A and IL-17RA interactions with a linear peptide. Sci. Rep. 6, 26071.

Liu, L., Wang, P., Nair, M.S., Yu, J., Rapp, M., Wang, Q., Luo, Y., Chan, J.F., Sahi, V., Figueroa, A., et al. (2020). Potent neutralizing antibodies against multiple epitopes on SARS-CoV-2 spike. Nature 584, 450–456.

Liu, C., Ginn, H.M., Dejnirattisai, W., Supasa, P., Wang, B., Tuekprakhon, A., Nutalai, R., Zhou, D., Mentzer, A.J., Zhao, Y., Duyvesteyn, H.M.E., et al. (2021). Reduced neutralization of SARS-CoV-2 B.1.617 by vaccine and convalescent serum. Cell 184, 4220–4236.e13.

McCallum, M., De Marco, A., Lempp, F.A., Tortorici, M.A., Pinto, D., Walls, A.C., Beltramello, M., Chen, A., Liu, Z., Zatta, F., et al. (2021). N-terminal domain antigenic mapping reveals a site of vulnerability for SARS-CoV-2. Cell 184, 2332–2347.e16.

McLeod, B., Miura, K., Scally, S.W., Bosch, A., Nguyen, N., Shin, H., Kim, D., Volkmuth, W., Rämisch, S., Chichester, J.A., et al. (2019). Potent antibody lineage against malaria transmission elicited by human vaccination with Pfs25. Nat. Commun. 10, 4328.

Misasi, J., and Sullivan, N.J. (2021). Immunotherapeutic strategies to target vulnerabilities in the Ebolavirus glycoprotein. Immunity 54, 412–436.

Nielsen, S.C.A., Yang, F., Jackson, K.J.L., Hoh, R.A., Röltgen, K., Jean, G.H., Stevens, B.A., Lee, J.Y., Rustagi, A., Rogers, A.J., et al. (2020). Human B Cell Clonal Expansion and Convergent Antibody Responses to SARS-CoV-2. Cell Host Microbe 28, 516–525.e5.

Panousis, C., Dhagat, U., Edwards, K.M., Rayzman, V., Hardy, M.P., Braley, H., Gauvreau, G.M., Hercus, T.R., Smith, S., Sehmi, R., et al. (2016). CSL311, a novel, potent, therapeutic monoclonal antibody for the treatment of diseases mediated by the common β chain of the IL-3, GM-CSF and IL-5 receptors. MAbs 8, 436–453.

Pettersen, E.F., Goddard, T.D., Huang, C.C., Couch, G.S., Greenblatt, D.M., Meng, E.C., and Ferrin, T.E. (2004). UCSF Chimera—A visualization system for exploratory research and analysis. J. Comput. Chem. 25, 1605–1612.

Pettersen, E.F., Goddard, T.D., Huang, C.C., Meng, E.C., Couch, G.S., Croll, T.I., Morris, J.H., and Ferrin, T.E. (2021). UCSF ChimeraX: Structure visualization for researchers, educators, and developers. Protein Sci. 30, 70–82.

Piccoli, L., Park, Y.J., Tortorici, M.A., Czudnochowski, N., Walls, A.C., Beltramello, M., Silacci-Fregni, C., Pinto, D., Rosen, L.E., Bowen, J.E., et al. (2020). Mapping neutralizing and immunodominant sites on the SARS-CoV-2 spike receptor-binding domain by structure-guided high-resolution serology. Cell 183, 1024–1042.e21.

Punjani, A., Rubinstein, J.L., Fleet, D.J., and Brubaker, M.A. (2017). cryoSPARC: algorithms for rapid unsupervised cryo-EM structure determination. Nat. Methods 14, 290–296.

Pymm, P., Adair, A., Chan, L.J., Cooney, J.P., Mordant, F.L., Allison, C.C., Lopez, E., Haycroft, E.R., O'Neill, M.T., Tan, L.L., et al. (2021). Nanobody cocktails potently neutralize SARS-CoV-2 D614G N501Y variant and protect mice. Proc. Natl. Acad. Sci. USA 118, e2101918118.

Rapp, M., Guo, Y., Reddem, E.R., Yu, J., Liu, L., Wang, P., Cerutti, G., Katsamba, P., Bimela, J.S., Bahna, F.A., et al. (2021). Modular basis for potent SARS-CoV-2 neutralization by a prevalent VH1-2-derived antibody class. Cell Rep. 35, 108950.

Robbiani, D.F., Gaebler, C., Muecksch, F., Lorenzi, J.C.C., Wang, Z., Cho, A., Agudelo, M., Barnes, C.O., Gazumyan, A., Finkin, S., et al. (2020). Convergent antibody responses to SARS-CoV-2 in convalescent individuals. Nature 584, 437–442.

Rocca, A., Biagi, C., Scarpini, S., Dondi, A., Vandini, S., Pierantoni, L., and Lanari, M. (2021). Passive immunoprophylaxis against respiratory syncytial virus in children: Where are we now? Int. J. Mol. Sci. 22, 3703.

Rogers, T.F., Zhao, F., Huang, D., Beutler, N., Burns, A., He, W.T., Limbo, O., Smith, C., Song, G., Woehl, J., et al. (2020). Isolation of potent SARS-CoV-2 neutralizing antibodies and protection from disease in a small animal model. Science 369, 956–963.

Saunders, K.O. (2019). Conceptual approaches to modulating antibody effector functions and circulation half-life. Front. Immunol. *10*, 1296.

Schäfer, A., Muecksch, F., Lorenzi, J.C.C., Leist, S.R., Cipolla, M., Bournazos, S., Schmidt, F., Maison, R.M., Gazumyan, A., Martinez, D.R., et al. (2021). Antibody potency, effector function, and combinations in protection and therapy for SARS-CoV-2 infection in vivo. J. Exp. Med. *218*, e20201993.

Subbarao, K., McAuliffe, J., Vogel, L., Fahle, G., Fischer, S., Tatti, K., Packard, M., Shieh, W.J., Zaki, S., and Murphy, B. (2004). Prior infection and passive transfer of neutralizing antibody prevent replication of severe acute respiratory syndrome coronavirus in the respiratory tract of mice. J. Virol. *78*, 3572–3577.

Tan, T.J.C., Yuan, M., Kuzelka, K., Padron, G.C., Beal, J.R., Chen, X., Wang, Y., Rivera-Cardona, J., Zhu, X., Stadtmueller, B.M., et al. (2021). Sequence signatures of two IGHV3-53/3-66 public clonotypes to SARS-CoV-2 receptor binding domain. Nat. Commun. *12*, 3815.

Taylor, P.C., Adams, A.C., Hufford, M.M., de la Torre, I., Winthrop, K., and Gottlieb, R.L. (2021). Neutralizing monoclonal antibodies for treatment of COVID-19. Nat. Rev. Immunol. *21*, 382–393.

Tiller, T., Meffre, E., Yurasov, S., Tsuiji, M., Nussenzweig, M.C., and Wardemann, H. (2008). Efficient generation of monoclonal antibodies from single human B cells by single cell RT-PCR and expression vector cloning. J. Immunol. Methods *329*, 112–124.

Tortorici, M.A., Beltramello, M., Lempp, F.A., Pinto, D., Dang, H.V., Rosen, L.E., McCallum, M., Bowen, J., Minola, A., Jaconi, S., et al. (2020). Ultrapotent human antibodies protect against SARS-CoV-2 challenge via multiple mechanisms. Science *370*, 950–957.

Voss, W.N., Hou, Y.J., Johnson, N.V., Delidakis, G., Kim, J.E., Javanmardi, K., Horton, A.P., Bartzoka, F., Paresi, C.J., Tanno, Y., et al. (2021). Prevalent, protective, and convergent IgG recognition of SARS-CoV-2 non-RBD spike epitopes. Science *372*, 1108–1112.

Wang, C., van Haperen, R., Gutiérrez-Álvarez, J., Li, W., Okba, N.M.A., Albulescu, I., Widjaja, I., van Dieren, B., Fernandez-Delgado, R., Sola, I., et al. (2021a). A conserved immunogenic and vulnerable site on the coronavirus spike protein delineated by cross-reactive monoclonal antibodies. Nat. Commun. *12*, 1715.

Wang, P., Casner, R.G., Nair, M.S., Wang, M., Yu, J., Cerutti, G., Liu, L., Kwong, P.D., Huang, Y., Shapiro, L., and Ho, D.D. (2021b). Increased resistance of SARS-CoV-2 variant P.1 to antibody neutralization. Cell Host Microbe *29*, 747–751.e4.

Wang, P., Nair, M.S., Liu, L., Iketani, S., Luo, Y., Guo, Y., Wang, M., Yu, J., Zhang, B., Kwong, P.D., et al. (2021c). Antibody resistance of SARS-CoV-2 variants B.1.351 and B.1.1.7. Nature *593*, 130–135.

Wang, Z., Schmidt, F., Weisblum, Y., Muecksch, F., Barnes, C.O., Finkin, S., Schaefer-Babajew, D., Cipolla, M., Gaebler, C., Lieberman, J.A., et al. (2021d). mRNA vaccine-elicited antibodies to SARS-CoV-2 and circulating variants. Nature *592*, 616–622.

Weisblum, Y., Schmidt, F., Zhang, F., DaSilva, J., Poston, D., Lorenzi, J.C., Muecksch, F., Rutkowska, M., Hoffmann, H.H., Michailidis, E., et al. (2020). Escape from neutralizing antibodies by SARS-CoV-2 spike protein variants. eLife *9*, e61312.

Williams, C.J., Headd, J.J., Moriarty, N.W., Prisant, M.G., Videau, L.L., Deis, L.N., Verma, V., Keedy, D.A., Hintze, B.J., Chen, V.B., et al. (2018). MolProbity: More and better reference data for improved all-atom structure validation. Protein Sci. *27*, 293–315.

Winkler, E.S., Gilchuk, P., Yu, J., Bailey, A.L., Chen, R.E., Chong, Z., Zost, S.J., Jang, H., Huang, Y., Allen, J.D., et al. (2021). Human neutralizing antibodies against SARS-CoV-2 require intact Fc effector functions for optimal therapeutic protection. Cell *184*, 1804–1820.e1816.

Winn, M.D., Ballard, C.C., Cowtan, K.D., Dodson, E.J., Emsley, P., Evans, P.R., Keegan, R.M., Krissinel, E.B., Leslie, A.G.W., McCoy, A., et al. (2011). Overview of the CCP4 suite and current developments. Acta Crystallogr. D Biol. Crystallogr. *67*, 235–242.

Wu, N.C., Yuan, M., Liu, H., Lee, C.D., Zhu, X., Bangaru, S., Torres, J.L., Caniels, T.G., Brouwer, P.J.M., van Gils, M.J., et al. (2020). An alternative binding mode of IGHV3-53 antibodies to the SARS-CoV-2 receptor binding domain. Cell Rep. *33*, 108274.

Yan, Q., He, P., Huang, X., Luo, K., Zhang, Y., Yi, H., Wang, Q., Li, F., Hou, R., Fan, X., et al. (2021). Germline IGHV3-53-encoded RBD-targeting neutralizing antibodies are commonly present in the antibody repertoires of COVID-19 patients. Emerg. Microbes Infect. *10*, 1097–1111.

Yuan, M., Wu, N.C., Zhu, X., Lee, C.D., So, R.T.Y., Lv, H., Mok, C.K.P., and Wilson, I.A. (2020a). A highly conserved cryptic epitope in the receptor binding domains of SARS-CoV-2 and SARS-CoV. Science *368*, 630–633.

Yuan, M., Liu, H., Wu, N.C., Lee, C.D., Zhu, X., Zhao, F., Huang, D., Yu, W., Hua, Y., Tien, H., et al. (2020b). Structural basis of a shared antibody response to SARS-CoV-2. Science *369*, 1119–1123.

Yuan, M., Huang, D., Lee, C.D., Wu, N.C., Jackson, A.M., Zhu, X., Liu, H., Peng, L., Gils, M.J., Sanders, R.W., et al. (2021). Structural and functional ramifications of antigenic drift in recent SARS-CoV-2 variants. Science *373*, 818–823.

Zhang, K. (2016). Gctf: Real-time CTF determination and correction. J. Struct. Biol. *193*, 1–12.

Zheng, S.Q., Palovcak, E., Armache, J.P., Verba, K.A., Cheng, Y., and Agard, D.A. (2017). MotionCor2: anisotropic correction of beam-induced motion for improved cryo-electron microscopy. Nat. Methods *14*, 331–332.

Zhou, D., Dejnirattisai, W., Supasa, P., Liu, C., Mentzer, A.J., Ginn, H.M., Zhao, Y., Duyvesteyn, H.M.E., Tuekprakhon, A., Nutalai, R., et al. (2021). Evidence of escape of SARS-CoV-2 variant B.1.351 from natural and vaccine-induced sera. Cell *184*, 2348–2361.e6.

Zivanov, J., Nakane, T., Forsberg, B.O., Kimanius, D., Hagen, W.J., Lindahl, E., and Scheres, S.H. (2018). New tools for automated high-resolution cryo-EM structure determination in RELION-3. eLife *7*, e42166.

Zost, S.J., Gilchuk, P., Case, J.B., Binshtein, E., Chen, R.E., Nkolola, J.P., Schäfer, A., Reidy, J.X., Trivette, A., Nargi, R.S., et al. (2020a). Potently neutralizing and protective human antibodies against SARS-CoV-2. Nature *584*, 443–449.

Zost, S.J., Gilchuk, P., Chen, R.E., Case, J.B., Reidy, J.X., Trivette, A., Nargi, R.S., Sutton, R.E., Suryadevara, N., Chen, E.C., et al. (2020b). Rapid isolation and profiling of a diverse panel of human monoclonal antibodies targeting the SARS-CoV-2 spike protein. Nat. Med. *26*, 1422–1427.

Zuo, Y., Wang, P., Sun, J., Guo, S., Wang, G., Zuo, T., Fan, S., Zhou, P., Liang, M., Shi, X., et al. (2018). Complementary recognition of the receptor-binding site of highly pathogenic H5N1 influenza viruses by two human neutralizing antibodies. J. Biol. Chem. *293*, 16503–16517.

STAR★METHODS

KEY RESOURCES TABLE

REAGENT or RESOURCE	SOURCE	IDENTIFIER
Antibodies		
anti-human IgG-PE	Southern Biotech	Cat#9040-09
anti-human CD19 - ECD	Beckman Coulter	Cat#IM2708U
anti-human IgG-BV786	BD Biosciences	Cat#564230
anti-human IgD-Cy7PE	BD Biosciences	Cat#561314
Streptavidin - APC	ThermoFisher	Cat#S866
Streptavidin - PE	ThermoFisher	Cat#S868
anti-human CD20 Alexa700	BD Biosciences	Cat#560631
anti-human IgM-BUV395	BD Biosciences	Cat#563903
anti-human CD21-BUV737	BD Biosciences	Cat#564437
anti-human CD14-BV510	Biolegend	Cat#301841
anti-human CD3-BV510	BD Biosciences	Cat#740187
anti-human CD8a-BV510	Biolegend	Cat#301048
anti-human CD16-BV510	Biolegend	Cat#302047
anti-human CD10-BV510	Biolegend	Cat#312220
Streptavidin – BV510	BD Biosciences	Cat#563261
Live Dead Aqua Viability Dye	ThermoFisher	Cat#L34957
HRP-conjugated anti-human IgG	Sigma	Cat#T0440-1L
anti-SARS-CoV N antibody	Rockland	Cat#200-401-A50
goat anti-rabbit IgG	Abcam	Cat#ab6721
Bacterial and virus strains		
E. coli DH5a	ThermoFisher	Cat#18258012
SARS-CoV-2 (CoV/Australia/VIC/01/2020)	University of Melbourne	N/A
SARS-CoV-2/human/USA/WA-CDC-WA1/2020	Colorado State University	N/A
B.1.351 (CoV/Australia/QLD/1520/2020)	University of Melbourne	N/A
Biological samples		
COVID-19 convalescent patient samples	University of Melbourne	N/A
Chemicals and recombinant proteins		
Trypsin TPCK	Fisher Scientific	Cat#NC9783694
Recombinant RBD protein	University of Melbourne	In house
Recombinant SARS-CoV-2 spike protein	University of Melbourne	In house
Recombinant HCoV-HKU1 spike protein	University of Melbourne	In house
Recombinant SARS-CoV-2 NTD protein	University of Melbourne	In house
Recombinant SARS-CoV spike protein	University of Melbourne	In house
Recombinant SARS-CoV-2 spike B.1.1.7 protein	University of Melbourne	In house
Recombinant SARS-CoV-2 spike B.1.351 protein	University of Melbourne	In house
Recombinant SARS-CoV-2 spike P.1 protein	University of Melbourne	In house
Recombinant huACE2 protein	University of Melbourne	In house
TMB substrate	Sigma	Cat#T0440-1L

Continued

REAGENT or RESOURCE	SOURCE	IDENTIFIER
Deposited data		
SARS-CoV-2 receptor binding domain bound to Fab PDI 210	This Paper	PDB: 7MZL
SARS-CoV-2 receptor binding domain bound to Fab PDI 42	This Paper	PDB: 7MZG
SARS-CoV-2 receptor binding domain bound to Fab PDI 215	This Paper	PDB: 7MZM
SARS-CoV-2 receptor binding domain bound to Fab WCSL 129 and Fab PDI 96	This Paper	PDB: 7MZK
SARS-CoV-2 receptor binding domain bound to Fab WCSL 129 and Fab PDI 93	This Paper	PDB: 7MZJ
SARS-CoV-2 receptor binding domain bound to Fab PDI 231	This Paper	PDB: 7MZN
SARS-CoV-2 receptor binding domain bound to Fab WCSL 129	This Paper	PDB: 7MZI
SARS-CoV-2 receptor binding domain bound to Fab WCSL 119	This Paper	PDB: 7MZH
SARS-CoV-2 receptor binding domain bound to Fab PDI 37	This Paper	PDB: 7MZF
SARS-CoV-2 receptor binding domain bound to Fab PDI 222	This Paper	PDB: 7RR0 EMDB: 24649
SARS-CoV-2 Spike bound to Fab PDI 210	This Paper	EMDB: 24642
SARS-CoV-2 Spike bound to Fab PDI 96	This Paper	EMDB: 24643
SARS-CoV-2 Spike bound to Fab PDI 215	This Paper	EMDB: 24644
SARS-CoV-2 Spike bound to Fab WCSL 119	This Paper	EMDB: 24645
SARS-CoV-2 Spike bound to Fab WCSL 129	This Paper	EMDB: 24646
SARS-CoV-2 Spike bound to Fab PDI 93	This Paper	EMDB: 24647
SARS-CoV-2 Spike bound to Fab PDI 222	This Paper	EMDB: 24648
Crystal structure of SARS-CoV-2 receptor binding domain in complex with human antibody CR3022	(Yuan et al., 2020a)	PDB: 6W41
Crystal structure of SARS-CoV-2 receptor binding domain in complex with neutralizing antibody CC12.3	(Yuan et al., 2020b)	PDB: 6XC4
Crystal structure of Z004 iGL Fab in complex with ZIKV EDIII	(Esswein et al., 2020)	PDB: 6UTA
Mapping neutralizing and immunodominant sites on the SARS-CoV-2 spike receptor-binding domain by structure-guided high-resolution serology	(Piccoli et al., 2020)	PDB: 7JXC
Crystal structure of the Fab fragment of the human neutralizing anti-West Nile Virus mAb CR4354	(Kaufmann et al., 2010)	PDB: 3N9G
Crystal structure of VRC01c-HuGL2 Fab from an HIV-1 naive donor in complex with with a germline-targeting gp120 engineered outer domain eOD-GT8 at 2.16 A	(Jardine et al., 2016)	PDB: 5IES
VH1-69 germline antibody with CDR H3 sequence of CR9114	https://doi.org/10.2210/pdb5WL2/pdb	PDB: 5WL2
Inhibiting complex IL-17A and IL-17RA interactions with a linear peptide	(Liu et al., 2016)	PDB: 5HHV
Crystal structure of influenza A virus H5 hemagglutinin globular head in complex with the Fab of antibody FLD21.140	(Zuo et al., 2018)	PDB: 6A67

Continued

REAGENT or RESOURCE	SOURCE	IDENTIFIER
Structure of the human 4-1BB / Urelumab Fab complex	(Chin et al., 2018)	PDB: 6MHR
Crystal Structure of ABBV-323 FAB	(Argiriadi et al., 2019)	PDB: 6PE7
Crystal structure of the SARS-CoV-2 RBD in complex with BD-236 Fab	(Du et al., 2020)	PDB: 7CHB
Pfs25 in complex with the human transmission blocking antibody 2530	(McLeod et al., 2019)	PDB: 6PHB
Crystal structure of SARS-CoV-2 receptor binding domain in complex with neutralizing antibody COVA2-39	(Wu et al., 2020)	PDB: 7JMP
Experimental models: Cell lines		
Expi293F	Thermo Fisher Scientific	Cat#A 14527
ExpiCHO	Thermo Fisher Scientific	Cat# A29127
Experimental models: Organisms/strains		
C57BL/6J Mice	The Walter and Eliza Hall Institute	N/A
Golden Syrian Hamster	Envigo, USA	Strain HsdHan®:AURA
Oligonucleotides		
5'-ATGGACTGGACCTGGAGGAT-3'	(Tiller et al., 2008)	Custom Synthesis
5'-ATGGACTGGACCTGGAGCAT-3'	(Tiller et al., 2008)	Custom Synthesis
5'-ATGGACTGGACCTGGAGAAT-3'	(Tiller et al., 2008)	Custom Synthesis
5'-GGTTCCTCTTTGTGGTGGC-3'	(Tiller et al., 2008)	Custom Synthesis
5'-ATGGACTGGACCTGGAGGGT-3'	(Tiller et al., 2008)	Custom Synthesis
5'-ATGGACTGGATTTGGAGGAT-3'	(Tiller et al., 2008)	Custom Synthesis
5'-AGGTTCCTCTTTGTGGTGGCAG-3'	(Tiller et al., 2008)	Custom Synthesis
5'-GGAAGGTGTGCACGCCGCTGGTC-3'	(Tiller et al., 2008)	Custom Synthesis
5'-TAAAAGGTGTCCAGTGT-3'	(Tiller et al., 2008)	Custom Synthesis
5'-TAAGAGGTGTCCAGTGT-3'	(Tiller et al., 2008)	Custom Synthesis
5'-TAGAAGGTGTCCAGTGT-3'	(Tiller et al., 2008)	Custom Synthesis
5'-TACAAGGTGTCCAGTGT-3'	(Tiller et al., 2008)	Custom Synthesis
5'-TTAAAGCTGTCCAGTGT-3'	(Tiller et al., 2008)	Custom Synthesis
5'-ATGAAACATCTGTGGTTCTT-3'	(Tiller et al., 2008)	Custom Synthesis
5'-TTCTCCAAGGAGTCTGT-3'	(Tiller et al., 2008)	Custom Synthesis
5'-GGAAGGTGTGCACGCCGCTGGTC-3'	(Tiller et al., 2008)	Custom Synthesis
5'-ATGAAACACCTGTGGTTCTTCC-3'	(Tiller et al., 2008)	Custom Synthesis
5'-ATGAAACACCTGTGGTTCTT-3'	(Tiller et al., 2008)	Custom Synthesis
5'-ATGAAGCACCTGTGGTTCTT-3'	(Tiller et al., 2008)	Custom Synthesis
5'-CCTCCACAGTGAGAGTCTG-3'	(Tiller et al., 2008)	Custom Synthesis
5'-ATGTCTGTCTCCTTCCTCATC-3'	(Tiller et al., 2008)	Custom Synthesis
5'-GGCAGCAGCAACAGGTGCCCA-3'	(Tiller et al., 2008)	Custom Synthesis
5'-GCTATTTTTAAAGGTGTCCAGTGT-3'	(Tiller et al., 2008)	Custom Synthesis
5'-GGAAGGTGTGCACGCCGCTGGTC-3'	(Tiller et al., 2008)	Custom Synthesis
5'-ATGAGGSTCCCYGCTCAGCTGCTGG-3'	(Tiller et al., 2008)	Custom Synthesis
5'-CTCTTCCTCCTGCTACTCTGGCTCCCAG-3'	(Tiller et al., 2008)	Custom Synthesis
5'-ATTTCTCTGTTGCTCTGGATCTCTG-3'	(Tiller et al., 2008)	Custom Synthesis
5'-GTTTCTCGTAGTCTGCTTTGCTCA-3'	(Tiller et al., 2008)	Custom Synthesis
5'-GGTCCTGGGCCCAGTCTGTGCTG-3'	(Tiller et al., 2008)	Custom Synthesis
5'-GGTCCTGGGCCCAGTCTGCCCTG-3'	(Tiller et al., 2008)	Custom Synthesis
5'-GCTCTGTGACCTCCTATGAGCTG-3'	(Tiller et al., 2008)	Custom Synthesis
5'-GGTCTCTCTCSCAGCYTGTGCTG-3'	(Tiller et al., 2008)	Custom Synthesis

Continued

REAGENT or RESOURCE	SOURCE	IDENTIFIER
5'-GTTCTTGGGCCAATTTTATGCTG-3'	(Tiller et al., 2008)	Custom Synthesis
5'-GGTCCAATTCYCAGGCTGTGGTG-3'	(Tiller et al., 2008)	Custom Synthesis
5'-GAGTGGATTCTCAGACTGTGGTG-3'	(Tiller et al., 2008)	Custom Synthesis
5'-CACCAGTGTGGCCTTGTTGGCTTG-3'	(Tiller et al., 2008)	Custom Synthesis
5'-ACAGGTGCCCACTCCCAGGTGCAG-3'	(Tiller et al., 2008)	Custom Synthesis
5'-AAGGTGTCCAGTGTGARGTGCAG-3'	(Tiller et al., 2008)	Custom Synthesis
5'-CCCAGATGGGTCCTGTCCCA GGTGCAG-3'	(Tiller et al., 2008)	Custom Synthesis
5'-CAAGGAGTCTGTTCCGAGGTGCAG-3'	(Tiller et al., 2008)	Custom Synthesis
5'-GCAGCCACAGGTGCCCACTCC-3'	(Tiller et al., 2008)	Custom Synthesis
5'-CAGCAGCTACAGGCACCCACGC-3'	(Tiller et al., 2008)	Custom Synthesis
5'-GGCAGCAGCTACAGGTGTCCAGTCC-3'	(Tiller et al., 2008)	Custom Synthesis
5'-GCT ATT TTA AAA GGT GTC CAA TGT-3'	(Tiller et al., 2008)	Custom Synthesis
5'-GTG GCA GCT CCC AGA TGG GTC CTG TC-3'	(Tiller et al., 2008)	Custom Synthesis
5'-GTT GCA GTT TTA AAA GGT GTC CAG TG-3'	(Tiller et al., 2008)	Custom Synthesis
5'-GCT GTT CTC CAA GGA GTC TGT TCC-3'	(Tiller et al., 2008)	Custom Synthesis
5'-GTTCGGGGAAGTAGTCCTTGAC-3'	(Tiller et al., 2008)	Custom Synthesis
5'-TGACCCAGWCTCCABYCWCCCTG-3'	(Tiller et al., 2008)	Custom Synthesis
5'-GTGCTGTCCTTGCTGTCCTGCT-3'	(Tiller et al., 2008)	Custom Synthesis
5'-CTGCTACCGGTTCCTGGGCCCAG TCTGTGCTGACKCAG-3'	(Tiller et al., 2008)	Custom Synthesis
5'-CTGCTACCGGTTCCTGGGCCCAGT CTGCCCTGACTCAG-3'	(Tiller et al., 2008)	Custom Synthesis
5'-CTGCTACCGGTTCTGTGACCTCCTA TGAGCTGACWCAG-3'	(Tiller et al., 2008)	Custom Synthesis
5'-CTGCTACCGGTTCTCTCTCSCAGCYT GTGCTGACTCA-3'	(Tiller et al., 2008)	Custom Synthesis
5'-CTGCTACCGGTTCTTGGGCCAATTTT ATGCTGACTCAG-3'	(Tiller et al., 2008)	Custom Synthesis
5'-CTGCTACCGGTTCCAATTCYCAGRCT GTGGTGACYCAG-3'	(Tiller et al., 2008)	Custom Synthesis
5'-CTCCTCACTCGAGGGYGGGAACA GAGTG-3'	(Tiller et al., 2008)	Custom Synthesis
Recombinant DNA		
SARS-CoV-2 (Wuhan) Hexapro Spike expression plasmid	(Juno et al., 2020b)	AKW1462
SARS-CoV-2 RBD expression plasmid	Tan et al., 2021	AKW1063
SARS-CoV-2 NTD expression plasmid	This study	AKW1749
SARS-CoV RBD expression plasmid	(Juno et al., 2020b)	N/A
pCAGGS-RBD expression plasmid	(Amanat et al., 2020)	N/A
SARS-CoV-2 (B.1.351) Hexapro Spike expression plasmid	This Study	AKW1829
SARS-CoV-2 (B.1.1.7) Hexapro Spike expression plasmid	This Study	AKW1830
SARS-CoV-2 (P.1) Hexapro Spike expression plasmid	This Study	AKW1828
HCoV-HKU1 Spike 2P expression plasmid	(Juno et al., 2020b)	AKW1046

Continued

REAGENT or RESOURCE	SOURCE	IDENTIFIER
Software and algorithms		
Octet Data Analysis 10.0	Fortebio/Sartorius	N/A
Relion 3.1	Zivanov et al., 2018	https://relion.readthedocs.io/en/latest/
ChimeraX	Pettersen et al., 2021	https://www.cgl.ucsf.edu/chimerax/
Chimera v1.1.3	Pettersen et al., 2004	https://www.cgl.ucsf.edu/chimera/
Phenix v1.16	Liebschner et al., 2019	www.phenix-online.org
Coot v0.9.5	Emsley et al., 2010	https://www2.mrc-lmb.cam.ac.uk/personal/pemsley/coot/
PyMOL v2.3	The PyMOL Molecular Graphics System, Version 2.3 Schrödinger	https://pymol.org/2/
CryoSPARC v3.2	Structura Biotechnology, Punjani et al., 2017	https://cryosparc.com/download
Gautomatch v0.56	N/A	https://www.mrc-lmb.cam.ac.uk/kzhang/
PISA	European Bioinformatics Institute	https://www.ebi.ac.uk/pdbe/prot_int/pistart.html
CCP4 v7.1	Winn et al., 2011	https://www.ccp4.ac.uk
XDS	Kabsch, 2010	https://xds.mr.mpg.de
Other		
AKTA Pure	Cytiva	N/A
Octet 96e	ForteBio/Sartorius	N/A
Flexmap3D	Luminex Corporation	N/A
Streptavidin Dynabeads M-280	Invitrogen	Cat#112.06D

RESOURCE AVAILABILITY

Lead contact
Further information and requests for resources and reagents should be directed to and will be fulfilled by the lead contact, Wai-Hong Tham (tham@wehi.edu.au)

Materials availability
All requests for resources and reagents should be directed to and will be fulfilled by the Lead Contact author. This includes anti-bodies, plasmids, and proteins. All reagents will be made available on request after completion of a Materials Transfer Agreement.

Data and code availability
The structure data and the antibody sequences of the SARS-CoV-2 RBD bound to PDI 37, PDI 42, PDI 93, PDI 96, PDI 210, PDI 215, PDI 222, PDI 231, WCSL 119 and WCSL 129 are available at the PDB under accession codes 7MZF, 7MZG, 7MZJ, 7MZK, 7MZL, 7MZM, 7RR0, 7MZN, 7MZH and 7MZI respectively. Electron microscopy (EM) maps are available at the electron microscopy databank (EMDB) for SARS-CoV-2 Spike bound to PDI 93, PDI 96, PDI 210, PDI 215, PDI 222, WCSL 119 and WCSL 129 under accession codes EMDB-24647, EMDB-24643, EMDB-24642, EMDB-24644, EMDB-24648, EMDB-24645 and EMDB-24646 respectively. The EM map for PDI-222 binding the SARS-CoV-2 RBD is available under accession code EMDB-24649. This paper does not report original code. Any additional information required to reanalyse the data reported in this paper is available from the lead contact upon request.

EXPERIMENTAL MODEL AND SUBJECT DETAILS

Human subjects
Individuals recovered from COVID-19 (N = 64) were recruited through contacts with the investigators and invited to provide a blood sample. The study protocols were approved by the University of Melbourne Human Research Ethics Committee (#2056689) and all associated procedures were carried out in accordance with the approved guidelines. All participants provided written informed consent in accordance with the Declaration of Helsinki. The cohort screened for serological neutralisation activity had a median age of 55 (IQR:49 - 62) and were 43.8% female (28 of 64).

Mice
C57BL/6J mice were bred and housed at the Walter and Eliza Hall Institute of Medical Research. All procedures involving animals and live SARS-CoV-2 were conducted in an OGTR-approved Physical Containment Level 3 (PC-3) facility at the Walter and Eliza Hall

Institute of Medical Research (Cert-3621; IA88_20). All animal procedures were approved by The Walter and Eliza Hall Institute of Medical Research Animal Ethics Committee (2020.016). Mice used for experimentation were males of 7-10 weeks of age.

Hamsters
Golden Syrian Hamsters (*Mesocricetus auratus;* genotype: HsdHan: AURA) were sourced from Envigo, USA. All animals were male and ∼11 weeks old at time of challenge. All procedures involving were conducted under ethics approval #1035 and the oversight of the Colorado State University Institutional Animal Care and Use committee.

Cell lines
Chinese Hamster ovary cell line ExpiCHO-S™ (Thermo Fisher) and Human embryonic kidney fibroblast cell line Expi293F™ (Thermo Fisher) were used for mammalian expression of recombinant proteins for affinity measurements, crystallography and cryo-EM. Cells were maintained and transfected according to protocols in the ExpiCHO expression system™ kit (Thermo Fisher #A29133) and the Expi293 expression system™ kit (Thermo Fisher #A14635) respectively, with the addition of lupin peptone (Cell Biosciences #A230100) 24 hours post-transfection to Expi293F cells.

METHOD DETAILS

Sample collection
Whole blood was obtained with sodium heparin anticoagulant. Plasma was collected and stored at −80°C, and PBMCs were isolated via Ficoll-Paque separation, cryopreserved in 10% DMSO/FCS and stored in liquid nitrogen. Selection of the 6 subjects for isolation and sequencing of spike-specific B cells was based upon prior screening for potent plasma neutralising activity in a limiting dilution microneutralisation assay.

Generation of recombinant proteins
The generation of SARS-CoV-2 RBD, hACE2, HKU-1 spike and SARS-CoV RBD proteins for ELISA and/or flow cytometry has been previously described in detail (Juno et al., 2020b). A construct for expressing SARS-CoV-2 with six proline stabilization mutations (Hexapro) was synthesized and expressed as previously described (Hsieh et al., 2020). A construct for expressing NTD (residues 1 - 290) was synthesized with a C-terminal Avitag and polyhistidine tag. A construct for expressing SARS-CoV spike protein was synthesized containing 2P mutations and a C-terminal trimerization foldon, Avitag and polyhistidine tag. All coronavirus proteins were expressed using transient transfection of Expi293 or ExpiCHO cells and purified by Ni-NTA affinity and size-exclusion chromatography using a Superdex S75 increase 10/300 column or a Superose 6 16/70 column (Cytiva).

Limiting dilution microneutralisation assay
SARS-CoV-2 isolate CoV/Australia/VIC01/2020 was passaged in Vero cells and stored at −80°C. Plasma was heat-inactivated at 56°C for 30 min. Plasma was serially diluted 1:20 to 1:10240 before addition of 100 $TCID_{50}$ of SARS-CoV-2 in MEM/0.5% BSA and incubation at room temperature for 1 hour. Residual virus infectivity in the plasma/virus mixtures was assessed in quadruplicate wells of Vero cells incubated in serum-free media containing 1 μg/ml TPCK trypsin at 37°C/5% CO2; viral cytopathic effect was read on day 5 and neutralising antibody titer calculated using the Reed/Muench method as described (Subbarao et al., 2004).

Recovery of human monoclonal antibodies from SARS-CoV-2-specific B cells
Fluorescent B cell probes for identification of SARS-CoV-2 S-specific B cells within cryopreserved human PBMC were generated as described (Juno et al., 2020a). Cells were stained with Aqua viability dye (ThermoFisher) before incubation with B cell probes (Hexapro spike or RBD) and monoclonal antibodies for surface staining CD19-ECD (J3-119) (Beckman Coulter), CD20 Alexa700 (2H7), IgM-BUV395 (G20-127), CD21-BUV737 (B-ly4), IgD-Cy7PE (IA6-2), IgG-BV786 (G18-145) (BD), CD14-BV510 (M5E2), CD3-BV510 (OKT3), CD8a-BV510 (RPA-T8), CD16-BV510 (3G8), CD10-BV510 (HI10a) (Biolegend). Single antigen-specific class-switched B cells (S or RBD+, CD19+ IgD- IgG+) were sorted using a BD Aria II into 96-well plates, subject to cDNA generation and multiplex PCR and Sanger sequencing, as previously described (Juno et al., 2020a; Tiller et al., 2008). Productive, recombined heavy (V-D-J) and light (V-J) chain immunoglobulin sequences were synthesized (Geneart) and cloned into human IgG1 expression vectors for recombinant production in Expi293 mammalian cell culture using transient transfection. After 4–5 days, IgG1 was purified from culture supernatants using Protein-A affinity chromatography.

Phage library isolation of SARS-CoV-2 spike and RBD antibodies
Biopanning for SARS-CoV-2 spike and RBD human antibodies displayed in the CSL Human antibody phage library was performed as previously described (Panousis et al., 2016). Phages displaying SARS-CoV-2 spike and RBD specific Fabs were enriched after three rounds of biopanning on biotinylated SARS-CoV-2 spike or RBD protein immobilised to streptavidin Dynabeads (Dynal M-280, Invitrogen, cat # 112.06D). After the third round of panning, individual clones were selected for further analyses by ELISA for the presence of SARS-CoV-2 spike and RBD binding phage respectively. Positive clones were sequenced and annotated using the International ImMunoGeneTics database (IMGT) and aligned in Geneious Prime. Fabs from positive phage were reformatted into IgG1

expression plasmids and used to transiently transfect Expi293 cells. Human IgG1 antibodies were purified using Protein-A affinity chromatography.

Screening ELISA for phage library mAbs

96-well flat-bottomed MaxiSorp plates were coated with 50 μL of 125 nM recombinant protein in PBS at room temperature for one hour. All washes were done three times using PBS and 0.1% Tween (DPBS-T) and all incubations were performed for one hour at room temperature. Coated plates were washed and blocked by incubation with 4% skim milk solution. Plates were washed and then incubated with 50 μL of 125 nM IgG1. The plates were washed and incubated with horseradish peroxidase (HRP)-conjugated Goat anti-Human IgG secondary antibody (1:5000). After a final wash, 50 μL of azino-bis-3-ethylbenthiazoline-6-sulfonic acid (ABTS liquid substrate; Sigma) was added and incubated in the dark at room temperature for 20 minutes and 50 μL of 1% SDS was used to stop the reaction. Absorbance was read at 405 nm and all samples were done in duplicate.

Assessment of mAb binding specificity by ELISA

96-well Maxisorp plates (Thermo Fisher) were coated overnight at 4°C with 2 μg/mL recombinant SARS-CoV-2 S, SARS-CoV-2 RBD, SARS-CoV-2 NTD, SARS-CoV S, HKU-1 S or OC43 S proteins. After blocking with 1% FCS in PBS, antibodies diluted in PBS incubated for two hours and then washed prior to incubation with 1:20000 dilution of HRP-conjugated anti-human IgG (Sigma) for 1 hour. Plates were washed and developed using TMB substrate (Sigma), stopped using 0.16 M sulphuric acid and read at 450 nm. Effective concentration midpoints (EC_{50}) concentrations were calculated using a fitted curve (4 parameter log regression) and Prism 9.0 software (Graphpad).

ACE2-RBD inhibition ELISA

An ELISA was performed to measure the ability of antibodies to block interaction between recombinant human ACE2 and RBD proteins. 96-well Maxisorp plates (Thermo Fisher) were coated overnight at 4°C with 2.5 μg/ml of recombinant RBD protein in carbonate-bicarbonate coating buffer (Sigma). After blocking with PBS containing 1% BSA, duplicate wells of 2.5-fold serially diluted mAbs (from 5 μg/ml) were added and incubated for 1 hour at room temperature. Plates were then incubated with 1 μg/ml of biotinylated recombinant ACE2 protein for 1 hour at room temperature followed by incubation with HRP-conjugated streptavidin (ThermoFisher Scientific) for 1 hour at room temperature. Plates were developed with TMB substrate (Sigma), stopped with 0.15 M sulphuric acid and read at 450 nm.

Microneutralisation assay with ELISA-based read out

Wild-type SARS-CoV-2 (CoV/Australia/VIC/01/2020) and B.1.351 (CoV/Australia/QLD/1520/2020) isolates were passaged in Vero cells and stored at −80°C. 96-well flat bottom plates were seeded with Vero cells (20,000 cells per well in 100 μl). The next day, Vero cells were washed once with 200 μl serum-free DMEM and added with 150 μl of infection media (serum-free DMEM with 1.33 μg/ml TPCK trypsin). 2-fold serial dilutions of mAbs (from 5 μg/ml) were incubated with WT and B.1.351 SARS-CoV-2 isolates at 2000 $TCID_{50}$/ml at 37°C for 1 hour. Next, mAb-virus mixtures (50 μl) were added to Vero cells in duplicate and incubated at 37°C for 48 hours. 'Cells only' and 'virus+cells' controls were included to represent 0% and 100% infectivity respectively. After 48 hours, all cell culture media were carefully removed from wells and 200 μl of 4% formaldehyde was added to fix the cells for 30 mins at room temperature. The plates were then dunked in a 1% formaldehyde bath for 30 minutes to inactivate any residual virus prior to removal from the BSL3 facility. Cells were washed once in PBS and then permeabilised with 150 μl of 0.1% Triton-X for 15 minutes. Following one wash in PBS, wells were blocked with 200 μl of blocking solution (4% BSA with 0.1% Tween-20) for 1 hour. After three washes in PBST (PBS with 0.05% Tween-20), wells were added with 100 μl of rabbit polyclonal anti-SARS-CoV N antibody (Rockland, #200-401-A50) at a 1:8000 dilution in dilution buffer (PBS with 0.2% Tween-20, 0.1% BSA and 0.5% NP-40) for 1 hour. Plates were then washed six times in PBST and added with 100 μl of goat anti-rabbit IgG (Abcam, #ab6721) at a 1:8000 dilution for 1 hour. After six washes in PBST, plates were developed with TMB and stopped with 0.15 M H_2SO_4. OD values read at 450 nm were then used to calculate %neutralisation with the following formula: ('Virus + cells' – 'sample') ÷ ('Virus + cells' – 'Cells only') × 100. IC_{50} values were determined using four-parameter nonlinear regression in GraphPad Prism with curve fits constrained to have a minimum of 0% and maximum of 100% neutralisation.

Affinity measurements using bio-layer interferometry

Affinity determination measurements were performed on the Octet RED96e (ForteBio). Assays were performed at 25°C in solid black 96-well plates agitated at 1000 rpm. Kinetic buffer was composed of PBS pH 7.4 supplemented with 0.1% (w/v) BSA and 0.05% (v/v) TWEEN-20. All assays were performed using anti-human IgG Fc capture sensor tips (AHC) sensors (ForteBio). A 60 s biosensor baseline step was applied before human antibodies (5 μg/mL) were loaded onto AHC sensors. For affinity measurements against SARS-CoV-2 RBD, antibodies were loaded by submerging sensor tips for 200 s and then washed in kinetics buffer for 60 s. Association measurements were performed by dipping into a two-fold dilution series of SARS-CoV-2 RBD from 6 - 200 nM for 180 s and dissociation was measured in kinetics buffer for 180 s. For affinity measurements against SARS-CoV-2 spike, antibodies were loaded by submerging sensor tips until a response of 0.5 nm then washed in kinetics buffer for 60 s. Association measurements were performed by dipping into a two-fold dilution series of SARS-CoV-2 spike from 3 – 100 nM for 180 s and dissociation was measured in kinetics

24 hours later under ketamine-xylazine anesthesia by intranasal instillation of 100 μL of SARS-CoV-2 (strain SARS-CoV-2/human/USA/WA-CDC-WA1/2020). From 2 days prior to challenge until euthanasia, hamsters were evaluated clinically and weighed. An equal number of hamsters from each treatment group was necropsied 3 d after challenge, ~100 mg of right cranial and right caudal lung lobes and nasal tissues was excised, immersed in 0.9 mL of BA1/FBS, and homogenized. Tissue homogenates were frozen at −80°C. Virus titrations were performed using a double-overlay plaque assay on Vero E6 cells in 6-well plates. Briefly, serial 10-fold dilutions of tissue homogenates were inoculated onto cells and incubated 45 min, and 2 mL of a first overlay (0.5% agarose in MEM) without neutral red was added to each well. A second 2 mL overlay containing 0.06 mg/ml neutral red was added after 1 day and plaques were counted after an additional 1 and 2 d.

Crystallography

Fab fragments were generated from full length IgG1 antibodies through cleavage with IgG degrading enzyme E (IGDE) for 16-24 hours at 37°C. Fab fragments were purified using Lambda and Kappa Select columns (Cytiva) per the manufacturer's protocol. Complexes of SARS-CoV-2 RBD bound to Fab fragments were purified via SEC in 20 mM HEPES pH 7.5, 150 mM NaCl. Crystallization trials were set up with protein concentrations of 8 and 4 mg/ml at the Collaborative Crystallization Centre at Commonwealth Scientific and Industrial Research Organization (CSIROC3, Parkville) at 20°C. Crystals of SARS-CoV-2 RBD- PDI 37 appeared in 0.2 M ammonium sulfate, 20% PEG3350, 0.1 M Tris-chloride pH 8.5 and were harvested with mother liquor containing 25% glycerol. SARS-CoV-2 RBD-PDI 42 crystals were obtained in 10% PEG8000, 0.2 M NaCl, 0.1 M sodium dihydrogen-dipotassium hydrogen phosphate pH 6.2 and were flash frozen in mother liquor containing 30% glycerol. Crystals of SARS-CoV-2 RBD-PDI 210 appeared in 15% PEG6000, 0.1% (w/v) n-Octyl-b-D-glucoside and crystals of SARS-CoV-2 RBD-WCSL 129- PDI 96 grew in 0.1 M Tri-sodium citrate pH 5.5, 10% PEG8000. These crystals were flash frozen in mother liquor containing 20% glycerol or 20% 2-Methyl-2,4-pentanediol, respectively.

Hanging drop vapor diffusion crystallization trials were performed in-house for crystal optimization of SARS-CoV-2 RBD bound to WCSL 119, WCSL 129, WCSL 129- PDI 93, PDI 215, and PDI 231. Diffraction quality crystals of SARS-CoV-2 RBD-WCSL 119 crystals grew in 14% PEG3350, 0.2 M potassium thiocyanate seeded from initial screens and were stepwise transferred into cryo-protectant containing 30% ethylene glycol. SARS-CoV-2 RBD-WCSL 129 were obtained in 18% PEG3350, 0.1 M tri sodium citrate pH 5.5 seeded from initial screens and were harvested with 30% glycerol in mother liquor. A crystallization plate of SARS-CoV-2 RBD-PDI 215 was incubated at 4°C for 48 hours and subsequently transferred to 20°C. Crystals appeared after 2 days in 12% isopropanol, 12% PEG4000, 0.1 M tri sodium citrate pH 5.6 seeded from initial screens and were flash frozen in mother liquor containing 30% glycerol. SARS-CoV-2 RBD-WCSL 129- PDI 93 crystals grew in 23% PEG3350, 0.1 M sodium acetate pH 4.5 seeded from initial screens and SARS-CoV-2 RBD-PDI 231 crystals in 18% PEG3350, 10% N,N-Dimethyldodecylamine N-oxide (LDAO), 0.2 M sodium sulfate seeded from initial screens. Mother liquor containing 6% glycerol was used as cryo-protectant for SARS-CoV-2 RBD-WCSL 129-PDI 93 and mother liquor containing 20% butanediol was used for SARS-CoV-2 RBD-PDI 231 crystals.

X-ray diffraction data was collected at the MX2 beamline at the Australian Synchrotron, recorded with an Eiger 16M detector (Dectris) and processed using the XDS package (Kabsch, 2010). Molecular replacement using Phaser (Winn et al., 2011) was performed to solve the phase problem. SARS-CoV-2 RBD (PDB ID 6W41) and Fab structures of high sequence similarity were use as search models (PDB ID 6XC4 (heavy chain, HC) and 6UTA (light chain, LC) for PDI 37, for PDI 42, 7JXC for PDI 93, 3N9G for PDI 96, 5IES (heavy chain, HC) and 5WL2 (light chain, LC) for WCSL 119, 5HHV (HC) and 6A67 (LC) for WCSL 129, 6MHR for PDI 210, 6PE7 for PDI 215, 7CHB (HC) and 6PHB (LC) for PDI 231). For complexes of SARS-2 RBD bound by two Fabs simultaneously (WCSL 129-PDI 93, or WCSL 129-PDI 96) coordinates of the previously solved SARS-CoV-2 RBD-WCSL 129 structure was used as a search model instead of PDB ID 6W41. Iterative rounds of model building and refinement were undertaken using COOT (Emsley et al., 2010) and Phenix (Liebschner et al., 2019). Figures of the complexes were prepared using the PyMOL Molecular Graphics System, Version 2.3.0 (Schrödinger, LLC). Interactions, interfaces and buried areas from solvent were analyzed using PDBePISA v1.52 (Krissinel and Henrick, 2007). The atomic coordinates and structure factor files have been deposited in the Protein Data Bank. Accession numbers are listed in the crystallographic Table S3.

Cryo-EM sample preparation and data acquisition

The pre-fusion stabilized spike trimer (Hexapro) was purified over SEC and concentrated to 2.5 mg/ml. Fab fragments of human IgG1 antibodies PDI 93, PDI 96, PDI 210, PDI 215, PDI 222, WCSL 119 and WCSL 129 were purified over SEC and concentrated to 6 mg/ml. Prior to grid preparation spike trimer was incubated with a Fab fragment at a 4:1 molar ratio for 30 minutes at room temperature. The grids (Quantifoil Cu R1.2/1.3) were glow discharged in air at 10 mA for 90 s using Pelco EasyGlow. The 3 μl samples were applied to the grids at 4°C and 100% humidity and plunge frozen in liquid ethane using Vitrobot Mark IV (Thermo Fisher Scientific, USA). Data was collected on Titan Krios (Thermo Fisher Scientific, USA) 300 kV electron microscope using K2 detector (Gatan, USA). The data were collected during three sessions.

In the first session datasets for antibody-Spike complexes for candidates PDI 96, PDI 210, WCSL 129, PDI 93 and PDI 222 were collected with 1049, 1008, 1003, 1063 and 723 movies respectively, each movie containing 50 frames at a pixel size of 1.8 Å and total exposure of 50.0 e/Å^2. In the second session datasets for antibody-Spike complexes for candidates PDI 215 and WCSL 119 were collected with 2395 and 1866 movies respectively, each movie containing 40 frames at a pixel size of 1.8 Å and total exposure of 52.2 e/Å^2. The acquisition for these two sessions was performed at 81K indicated magnification using the energy filter slit width of 15 eV. In

the third session a higher resolution dataset was collected for the PDI 222 antibody-Spike complex. This dataset was collected with 1900 movies, each movie containing 51 frames at a pixel size of 1.06 Å and total exposure of 50.0 e/Å^2. The acquisition was performed at 130K indicated magnification using the energy filter slit width of 15 eV. All data were collected using FEI EPU software using a 9-hole beam-image shift acquisition scheme with one exposure in each hole.

Cryo-EM data processing

Processing of medium-resolution datasets for PDI 96, PDI 210, WCSL 129, PDI 93 and PDI 222

All datasets were processed independently. Data collected in the first two sessions at moderate resolution (1.8 Å pixel size) were subjected to the correction of beam-induced motion using MotionCor2 (Zheng et al., 2017), followed by CTF estimation using Gctf (Zhang, 2016). Micrographs with CTF fit resolution below 6 Å were selected for further examination. Template-based particle picking was performed using Gautomatch (https://www.mrc-lmb.cam.ac.uk/kzhang/) using projections from EMDB 23566 low-pass filtered to 20 Å. Particle coordinates were imported into Relion 3.1 (Zivanov et al., 2018). Particle extraction using 2 x binned particles (112 pixel box size) yielded 892,966 (PDI 96), 939,575 (PDI 210), 959,431 (WCSL 129), 994,647 (PDI 93), 709,466 (PDI 222), 1,925,957 (WCSL 119) and 2,089,347 (PDI 215) particles.

All further processing for PDI 96, PDI 210, WCSL 129, PDI 93 and PDI 222 was performed in Relion 3.1. First, particles underwent 2D classification, good classes were selected and proceeded to 3D classification. Particles from the best 3D class or classes were reextracted without rescaling (224 pixel box size) and subjected to 3D refinement, resulting in datasets containing 214,450 (PDI 96), 381,942 (PDI 210), 238,812 (WCSL 129), 236,164 (PDI 93) and 176,819 (PDI 222) particles. Following post-processing, the final datasets gave maps in C1 symmetry between 4.07 Å and 4.43 Å (Table S4) based on the gold standard Fourier shell correlation cut-off of 0.143. Local resolution was determined using the internal local resolution procedure in Relion, using half-reconstructions as input maps.

Extracted and 2 x binned particles for WCSL 119 were imported into cryoSPARC 3.1.0, for 2D classification, ab-initio reconstruction and heterogeneous refinement (Punjani et al., 2017). At this point 329780 particles were exported back into Relion 3.1 for re-extraction without binning. Full-scale particles were imported again into cryoSPARC for homogeneous refinement with per-group CTF parameter optimization yielding a 4.11 Å map.

For PDI 215 2x binned particles were subject to multiple rounds of 2D classification in Relion 3.1 omitting the CTF until the first peak. After re-extraction without binning, the 17464 particles corresponding to Spike bound to PDI 215 were imported to cryoSPARC (Punjani et al., 2017), subjected to 2D classification and heterogeneous refinement (using the ab-initio generated model). The 11707 best particles were used for a homogeneous refinement with per-group CTF parameter optimization yielding 8.3 Å map. Local resolution for all maps was determined in Relion 3.1 with the internal local resolution procedure, using half-reconstructions as input maps.

High resolution data processing for PDI 222

The PDI 222 dataset collected at 1.06 Å pixel size was subjected to the correction of beam-induced motion using MotionCor2 (Zheng et al., 2017), followed by CTF estimation using Gctf (Zhang, 2016). Micrographs with CTF fit resolution below 4 Å were selected for further examination. Template-based particle picking was performed using Gautomatch (https://www.mrc-lmb.cam.ac.uk/kzhang/) using projections from EMDB 23566 low-pass filtered to 20 Å . Particle coordinates were imported into Relion 3.1 (Zivanov et al., 2018). Particle extraction yielded 522,835 particles binned to 220 pixels (2x binning).

Following 2D and 3D classification, 106927 particles were selected for further processing. Particles were reextracted without rescaling (440 pixel box size) and subjected to a 3D reconstruction using C1 symmetry, yielding a 3.58 Å resolution map. These data were further subjected to 2x rounds of Ctf Refinement (beam tilt, trefoil, 4th order aberrations, anisotropic magnification and per-particle defocus and astigmatism) and Bayesian Polishing (Zivanov et al., 2018). The 3D Refinement of "shiny" particles with C3 symmetry yielded a 2.82 Å resolution consensus map. All RBD appeared to be in the "up" position, however, the density of the Fabs was very poor due to the flexibility of RBD domains relative to the rest of the Spike. To overcome this, we performed focused refinement of an individual RBD bound to a variable Fab fragment (vfAb). First, to roughly overlay all RBD-fabs, the symmetry was expanded to C1 in Relion. Following symmetry expansion, the signal for 2 RBD-Fabs and the Spike N-terminal domains was subtracted and the remaining Spike with a single RBD domain bound to Fab was 3D refined to a resolution of 2.8 Å. This was followed by another round of signal subtraction leaving only the signal for a single remaining RBD bound to the Fab variable fragment (representing all Spike RBD-vfAb fragments aligned to each other). The 3D refinement with local searches yielded a 3 Åmap. To further improve map quality, particles were subjected to 2 rounds of 3D classification without alignments followed by masked 3D refinement with local searches. The final dataset of 182,255 particles yielded a 3.12 Å resolution map based on a gold standard Fourier shell correlation cut-off of 0.143. Local resolution was determined using the internal local resolution procedure in Relion, using half-reconstructions as input maps.

Model building

Following focused refinement, a high-resolution model was built using the PDI 222 - RBD map. The COVA2-39 RBD crystal structure (PDBID: 7JMP) was used for rigid-body docking of the RBD and vfAb following by iterative model adjustment and rebuilding in COOT (Emsley et al., 2010) and real-space refinement in PHENIX (Liebschner et al., 2019). Model validation was performed in MolProbity

(Williams et al., 2018). Figures were prepared using the PyMOL Molecular Graphics System, Version 2.3.0 (Schrödinger, LLC), Chimera v1.1.3 (Pettersen et al., 2004) and ChimeraX (Pettersen et al., 2021).

Statistical analyses

Grouped data are generally presented as median ± IQR, with groups compared by Mann-Whitney U tests using Prism 9.0 (Graphpad). Pairwise correlations were assessed using Spearmans tests in Prism 9.0 (Graphpad). All statistical details of experiments can be found in figure legends.